

## CHAPTER 1

# MODEL FOR FULLY NONLINEAR OCEAN WAVE SIMULATIONS DERIVED USING FOURIER INVERSION OF INTEGRAL EQUATIONS IN 3D

John Grue\* and Dorian Fructus

*Mechanics Division, Department of Mathematics  
University of Oslo, Norway*

*\*johng@math.uio.no*

We describe the basics of the mathematical derivations and numerical implementation of a pseudo-spectral method for fully nonlinear-dispersive simulations of ocean surface waves in three dimensions, and illustrate the method through practical computations. Special features of the method include analytical inversion of the Laplace equation by application of Fourier transform, analytical time integration of the linear part of the prognostic equations using one long time-step, and time-integration of the genuinely nonlinear part of the prognostic equations using auto-adaptive time-step control. The dominant evaluation of the Laplace equation solver is obtained in a FFT fashion and is useful for highly accurate simulations of strongly nonlinear waves propagating over large domains, while any accuracy is obtained by including a remaining contribution which is highly nonlinear and highly local in physical space. The effect of a bottom topography that is variable in space and time is fully accounted for. Computations of three-dimensional wave patterns, extreme events in long-crested seas and short wave formation due to long tsunamis running into shallow water are performed.

### 1. Introduction

Improved methods for the computation of fully nonlinear ocean surface waves serve many purposes. Activities measuring ocean surface phenomena use computer models as support for interpretation of the field data. Accurate phase resolved computations of nonlinear wave fields and wave induced orbital velocities are requested for subsequent statistical analysis and the modeling of long and short wave interaction. The wave fields in question typically take place in very large physical domains and over long

time windows. Another need relates to the safety of maritime and offshore activity, and to development projects in the coastal area. Current research in the broad area of marine hydrodynamics represents a strong and highly active development on international scale and is documented by the publications that are available on e.g. [www.iwwwf.org](http://www.iwwwf.org). The research in marine hydrodynamics requires a continued improvement of models for the non-linear wave motion that is input to advanced wave analysis of ships and offshore structures, and installations in the coastal area exposed to waves, e.g., clusters of fixed and floating wind turbines, active breakwaters for the protection of harbors, or other devices. Computation of very steep ocean waves represents a challenge in itself. The evolution of long wave fields and the effect of instability mechanisms have been focused in several studies following pioneering works by Benjamin and Feir<sup>1</sup> and Zakharov.<sup>2</sup> A review of the advances by the mid of 1980's can be found in Yuen and Lake.<sup>3</sup> Recent studies focus on instabilities, the formation of extreme wave events at sea – rogue waves, and how short-crested seas relax towards a steady state governed by the Tayfun distribution,<sup>4</sup> see e.g. Onorato et al.,<sup>5</sup> Dysthe et al.,<sup>6</sup> Socquet et al.<sup>7</sup>

The use of high-order spectral methods enables a relatively rapid modeling of the waves (West et al.,<sup>8</sup> Dommermuth and Yue,<sup>9</sup> Craig and Sulem<sup>10</sup>). Here, we describe a computational strategy in three dimensions that is based on extensive use of Fourier transform (Clamond and Grue,<sup>11</sup> Grue<sup>12</sup>) and with numerical implementation and convergence tested out (Fructus et al.,<sup>13</sup> Clamond et al.<sup>14,15</sup>). The method contains an auto-adaptive time integration procedure and fast converging iterative solution procedure of the Laplace equation. The dominant part of the solution is obtained by Fast Fourier Transform (FFT). The remaining highly nonlinear part have integrals with kernels that decay quickly in the space coordinate. In many applications involving the motion of moderately steep waves it suffices to evaluate the highly rapid FFT-part disregarding the slower part involving the integrals. The iterative method is so rapidly convergent that one iteration is sufficient for most practical applications. This means that the method is explicit. Any accuracy is obtained by a continued iteration, which has converged after three iterations.

The text is organized as follows, following the Introduction, section 2 provides the mathematical description of the method for wave motion in constant water depth and section 3 computations of three-dimensional patterns on the sea surface. Computations of extreme wave events with support from experimental results are compared to events in the field such

as the Camille and Draupner waves in section 4. The theory is extended to include the effect of a sea bottom that varies in space and time in section 5, relevant for modeling tsunami waves, while section 6 describes model computations of how short waves and solitons may form in shallow seas, such as the Strait of Malacca, due to a disaster wave such as the Indian Ocean tsunami. Finally, concluding remarks are given in section 7.

## 2. Numerical Integration of the Wave Field

### 2.1. Time integration procedure

Derivations follow references<sup>11–13,15</sup> where we assume that the velocity field of the fluid is derived by the gradient of a velocity potential  $\phi$  by  $\mathbf{v} = \text{grad } \phi$ , where  $\mathbf{v}$  denotes the fluid velocity. Cartesian coordinates are introduced by  $(\mathbf{x}, y)$ , where  $\mathbf{x} = (x_1, x_2)$  denotes the horizontal coordinate vector and  $y$  the vertical. In what follows  $t$  denotes time. At the free surface we work with the variables

$$\eta(\mathbf{x}, t), \quad \tilde{\phi}(\mathbf{x}, t) = \phi(\mathbf{x}, y = \eta, t), \quad V = \frac{\partial \phi}{\partial n} \sqrt{1 + |\nabla \eta|^2}, \quad (2.1)$$

where  $\eta$  denotes the elevation of the free surface,  $\tilde{\phi}$  the potential function at the free surface,  $V$  the normal velocity at the free surface multiplied by  $\sqrt{1 + |\nabla \eta|^2}$ , and  $\nabla = \partial/\partial x_1, \partial/\partial x_2$  the horizontal gradient. The normal vector points out of the fluid. The functions  $\eta$  and  $\tilde{\phi}$  are integrated forward in time by the prognostic equations which result from the kinematic and dynamic boundary conditions, giving

$$\eta_t - V = 0, \quad \tilde{\phi}_t + g\eta + \frac{|\nabla \tilde{\phi}|^2 - V^2 - 2V\nabla \eta \cdot \nabla \tilde{\phi} + |\nabla \eta \times \nabla \tilde{\phi}|^2}{2 + 2|\nabla \eta|^2} = 0, \quad (2.2)$$

where  $g$  denotes gravity. The time integration is performed in Fourier space, where the prognostic equations become

$$\mathcal{F}\{\eta\}_t - k\mathcal{F}\{\tilde{\phi}\} = \mathcal{F}\{N_1\}, \quad \mathcal{F}\{\tilde{\phi}\}_t + g\mathcal{F}\{\eta\} = \mathcal{F}\{N_2\}, \quad (2.3)$$

where  $\mathcal{F}\{N_1\} = \mathcal{F}\{V\} - k\mathcal{F}\{\tilde{\phi}\}$  and the expression for  $N_2$  equals the fraction corresponding to the third term on the left of the second equation in (2.2). The variables  $\mathcal{F}\{\eta\}$  and  $\mathcal{F}\{\tilde{\phi}\}$  are functions of time and wavenumber  $\mathbf{k}$  in spectral space. We introduce the variables  $\omega = \sqrt{gk \tanh kh}$ , where  $h$  denotes the water depth and  $k = |\mathbf{k}|$ , and  $\vec{Y} = [k\mathcal{F}\{\eta\}, k\omega\mathcal{F}\{\tilde{\phi}\}/g]^T$ , where

$T$  denotes transpose, and a matrix  $A$  by

$$A = \begin{bmatrix} 0 & -\omega \\ \omega & 0 \end{bmatrix}. \quad (2.4)$$

The prognostic equations become

$$\vec{Y}_t + A\vec{Y} = \vec{N}, \quad \vec{N} = [N_1, N_2]^T. \quad (2.5)$$

The linear part of the prognostic equations may be integrated analytically, which means that the linear part of the wave field is obtained at any time-instant  $t$  from the initial condition by using one (long) time-step. This is an advantage since the linear part of the equation contains the leading contribution to the motion while the nonlinear part is relatively smaller, and the applied time-step may be consequently be made larger. Another advantage relates to the stability of the integration. Thus we integrate instead

$$\vec{Y}(t) = \vec{Y}(t_0) \exp(-A(t - t_0)) + \int_{t_0}^t \exp A(s - t_0) \vec{N}(s) ds. \quad (2.6)$$

The second term of (2.6) is integrated using a Runge-Kutta (RK) scheme with a variable time-step where the latter is governed by a time-step control. This is done by estimating  $\vec{Y}$  at the next time instant using both fifth and fourth order RK-schemes evaluating the difference between the two. The procedure continues until this difference is less than a small, prescribed value. An auto-adaptive method that identifies an optimal step-size speeds up the time integration procedure.<sup>15</sup> The time-step varies according to the strength of nonlinearity of the wave field. An example showing the effect of the time-step control is illustrated in figure 6. We have experienced that constant-step methods, such as symplectic integrators, are inefficient as compared to a well calibrated variable time-stepping method. All physical quantities are represented on a grid which is twice as fine as the desired one. Nonlinear terms up to cubic order are evaluated in physical space, and the product is transformed to spectral space where the highest half of the Fourier modes are padded to zero. This represents the anti-aliasing strategy of the nonlinear terms.

## 2.2. Relation between $\eta$ , $\tilde{\phi}$ and $V = \phi_n \sqrt{1 + |\nabla \eta|^2}$

An additional relation between the variables  $\eta$ ,  $\tilde{\phi}$  and  $V$  at the free surface is required in order to integrate (2.6) forward in time. This relation comes from the solution of the Laplace equation in the fluid domain, and

is expressed here in terms of an integral equation involving the quantities at the free surface. In the first step we develop the integral equation for the simplest case, namely for water of infinite depth (the case of a finite, constant water depth is covered in the end of the paragraph, and the case of a sea bottom that may be variable both in space and time is covered in subsection 5), where we obtain

$$\int_S \frac{1}{r} \frac{\partial \phi'}{\partial n'} dS' = 2\pi \tilde{\phi} + \int_S \tilde{\phi}' \frac{\partial}{\partial n'} \left( \frac{1}{r} \right) dS'. \quad (2.7)$$

Here,  $S$  denotes the instantaneous free surface,  $n$  the normal at the free surface, pointing out of the fluid, and  $r$  the distance between the evaluation point,  $(\mathbf{x}, y)$ , and the integration point,  $(\mathbf{x}', y')$ , both at the free surface, i.e.  $r = \sqrt{R^2 + (y - y')^2}$ , where  $R = |\mathbf{x}' - \mathbf{x}|$ . For convenience we write  $\eta = \eta(\mathbf{x}, t)$ ,  $\eta' = \eta(\mathbf{x}', t)$ ,  $\tilde{\phi} = \tilde{\phi}(\mathbf{x}, t)$ ,  $\tilde{\phi}' = \tilde{\phi}'(\mathbf{x}', t)$ , and so on. Using that  $\phi_n dS = V d\mathbf{x}$  the integral equation becomes

$$\int_S \frac{V'}{r} d\mathbf{x}' = 2\pi \tilde{\phi} + \int_S \tilde{\phi}' \sqrt{1 + |\nabla \eta|^2} \frac{\partial}{\partial n'} \frac{1}{r} d\mathbf{x}'. \quad (2.8)$$

We introduce the variable  $D = (\eta' - \eta)/R$  corresponding to the difference in the wave elevation at two horizontal positions divided by the horizontal distance. In the case when  $R \rightarrow 0$  the quantity  $D$  tends to  $\partial D / \partial R$ . Thus, the distance  $r$  is expressed in terms of  $R$  and  $D$  by  $r = R[1 + D^2]^{1/2}$ , meaning that  $1/r = 1/R + 1/R[(1 + D^2)^{-1/2} - 1]$ . A reorganization of the equation gives

$$\int \frac{V'}{R} d\mathbf{x}' = 2\pi \tilde{\phi} + \dots - \int \frac{V'}{R} [(1 + D^2)^{-1/2} - 1] d\mathbf{x}', \quad (2.9)$$

where intergration is performed over the horizontal plane. Now we apply Fourier transform to the equation, giving, for the l.h.s.

$$\mathcal{F} \left\{ \int \frac{V'}{R} d\mathbf{x}' \right\} = \frac{2\pi}{k} \int V' e^{-i\mathbf{k}\cdot\mathbf{x}'} d\mathbf{x}' = \frac{2\pi \mathcal{F}\{V\}}{k}, \quad (2.10)$$

where  $\mathcal{F}$  denotes Fourier transform. This inverts the operator on the l.h.s. of the integral equation for  $V$ .<sup>11,12</sup> Introducing a decomposition of  $V$  by  $V = V_1 + V_2 + V_3 + V_4$ , we obtain the following expressions for the

components:

$$\mathcal{F}\{V_1\} = k\mathcal{F}\{\tilde{\phi}\}, \tag{2.11}$$

$$\mathcal{F}\{V_2\} = -k\mathcal{F}\{\eta V_1\} - \mathbf{ik} \cdot \mathcal{F}\{\eta \nabla \tilde{\phi}\}, \tag{2.12}$$

$$\mathcal{F}\{V_3\} = \frac{-k}{2\pi} \mathcal{F} \left\{ \int \tilde{\phi}' \left[ (1 + D^2)^{-\frac{3}{2}} - 1 \right] \nabla' \cdot \left[ (\eta' - \eta) \nabla' \frac{1}{R} \right] d\mathbf{x}' \right\}, \tag{2.13}$$

$$\mathcal{F}\{V_4\} = \frac{-k}{2\pi} \mathcal{F} \left\{ \int \frac{V'}{R} \left[ (1 + D^2)^{-\frac{1}{2}} - 1 \right] d\mathbf{x}' \right\}, \tag{2.14}$$

where we have used Gauss' theorem to arrive at the expression for  $V_2$ . While the contributions  $V_1, V_2, V_3$  are explicit, the term  $V_4$  is obtained in an implicit form. A good, leading approximation to the latter is obtained by introducing  $V_1 + V_2$  in the r.h.s. of the expression for  $V_4$ . This is the first step of an iterative procedure and is useful to obtain  $V_4$ . The procedure needs three iterations to be fully converged.<sup>13</sup>

It is of advantage to compute the leading contribution to  $V_4$  in the form of a global evaluation using Fourier transform, i.e.

$$\begin{aligned} \mathcal{F}\{\hat{V}_4\} &= \frac{k}{2\pi} \mathcal{F} \left\{ \int \frac{V' \frac{1}{2} D^2}{R} d\mathbf{x}' \right\} \\ &= -\frac{1}{2} k \mathcal{F}\{\eta^2 \mathcal{F}^{-1}[k\mathcal{F}(V)] - 2\eta \mathcal{F}^{-1}[k\mathcal{F}(\eta V)] + \mathcal{F}^{-1}[k\mathcal{F}(\eta^2 V)]\}, \end{aligned} \tag{2.15}$$

where  $\mathcal{F}^{-1}$  denotes inverse Fourier transform. In the computations the terms  $V_1 + V_2 + \hat{V}_4$  are evaluated using FFT. This sum constitutes the fast FFT-part of the method. The remaining integrals determined by  $V_3$  in eq. (2.13) above, and the difference,

$$\mathcal{F}\{V_4 - \hat{V}_4\} = \frac{-k}{2\pi} \mathcal{F} \left\{ \int \frac{V'}{R} \left[ (1 + D^2)^{-\frac{1}{2}} - 1 + \frac{1}{2} D^2 \right] d\mathbf{x}' \right\}, \tag{2.16}$$

are highly nonlinear and with kernels that decay rapidly with distance in the horizontal plane. These integrals have very local contributions and are evaluated by numerical integration over small domains in the horizontal plane, surrounding the field point  $\mathbf{x}$ .

In the case of a finite constant water depth,  $h$ , the Green function involved in the integral equation becomes  $1/r + 1/r_1$  where the latter is an image of the former with respect to the sea floor. The expression for  $\mathcal{F}(V)$  becomes

$$\begin{aligned} \mathcal{F}(V) &= kE_1 \mathcal{F}(\tilde{\phi}) - kE_1 \mathcal{F}(\eta V_1) - \mathbf{ik} \cdot \mathcal{F}(\eta \nabla \tilde{\phi}) \\ &\quad + kC_1 [\mathcal{F}(T(\tilde{\phi}) + T_1(\tilde{\phi})) + \mathcal{F}(N(V) + N_1(V))] \\ &\quad + kC_1 [e_1 \mathcal{F}(\eta(V - V_1)) + \mathcal{F}(\eta \mathcal{F}^{-1}(e_1 \mathcal{F}(V - V_1)))] \end{aligned} \tag{2.17}$$

where  $\mathcal{F}(V_1) = E_1 \mathcal{F}(\tilde{\phi})$ ,  $E_1 = \tanh kh$ ,  $C_1 = 1/(1 + e_1)$  and  $e_1 = \exp(-2kh)$ . The functions  $T$ ,  $N$ ,  $N_1$  and  $T_1$  are given in Grue,<sup>12</sup> eqs. (9), (10), (29), (30), respectively. This is the only modification to the time integration eq. (2.6) due to a finite constant water depth  $h$ .

### 2.3. Note on global and local integration

We note that, in cases when  $D^2 < 1$ , the term  $-(1 + D^2)^{-\frac{1}{2}} + 1$  in (2.14) has a convergent series expansion of the form,  $\frac{1}{2}D^2 - \frac{3}{8}D^4 + \frac{5}{16}D^6 + \dots$ ,  $D^2 < 1$ , where the infinite expansion can formally be used to rewrite the integral  $V_4$  obtaining a sum of convolutions. Such a procedure leads to the expansion suggested in the two-dimensional study by Craig and Sulem,<sup>10</sup> which, however, has essential drawbacks, including, among others: slow convergence; the convolution terms involving high-order derivatives lead to numerical instability; an inherent ill-conditioning due to cancellations. Our main conclusion is that the term is best divided into the sum  $\frac{1}{2}D^2 - \left[ (1 + D^2)^{-\frac{1}{2}} - 1 + \frac{1}{2}D^2 \right]$ , where the first term ( $\frac{1}{2}D^2$ ) contributes to a global evaluation using FFT and the second to a local, truncated integration. This subdivision is found to be insensitive to the magnitude of  $D^2$ . We have tested out another subdivision of the form  $\frac{1}{2}D^2 - \frac{3}{8}D^4 - \left[ (1 + D^2)^{-\frac{1}{2}} - 1 + \frac{1}{2}D^2 - \frac{3}{8}D^4 \right]$ , including also  $-\frac{3}{8}D^4$  in the global evaluation, and the remaining part as an even stronger local, truncated integration, but this was found to lead to a numerically unstable procedure.<sup>13</sup>

### 2.4. Comparison with other methods

Numerical integration of the evolution of long wave fields over long time using the 2D counterpart of the present method<sup>16</sup> showed excellent comparison with the method by West et al.,<sup>8</sup> but that the formulation of Dommermuth and Yue<sup>9</sup> was inaccurate in the long term in the numerical simulation and is caused by a poor representation of the vertical free surface velocity in the model.

## 3. Computations of Three-Dimensional Wave Patterns<sup>a</sup>

Three-dimensional wave structures may occur at the sea surface in the form of crescent-shaped patterns. These play an important role in wave

<sup>a</sup>This section 3 is a reprint of section 4 in chapter 4 (pp. 191-202) of Grue and Trulsen,<sup>17</sup> with kind permission given by CISM, and is gratefully acknowledged.

breaking and cause transfer of momentum and energy between the ocean and atmosphere. The three-dimensional structures may result from spontaneous instabilities of a two-dimensional water wave field. Particularly those emerging naturally from the instability of Stokes waves are considered here. The stability of Stokes waves has been studied for many decades. Two-dimensional instability was studied by Lighthill<sup>18</sup> and Benjamin and Feir,<sup>1</sup> working with triads – or the side-band instability, while Zakharov<sup>2</sup> also included three-dimensional instabilities in his analysis, working with quartets in the wavenumber space. Later, McLean et al.<sup>20</sup> and McLean<sup>21</sup> discovered a new kind of three-dimensional instability which, prior to this, had been suggested in a two-dimensional study by Longuet-Higgins.<sup>22</sup> The new instability analysis involved the interaction between quintets and higher resonances in the wavenumber space. We study here 5-wave and higher interactions.

### 3.1. *The stability analysis by McLean et al.*<sup>20</sup>

This analysis was motivated by experimental measurements of three-dimensional wave patterns by Su, later documented in Su,<sup>19</sup> and by preliminary calculations of the patterns by Saffman and Yuen, see reference 12 in McLean et al.<sup>20</sup> The research group, including McLean, Ma, Martin, Saffman and Yuen at the Fluid Mechanics Department, TRW Defense and Space Systems Group in California, performed analysis and computations demonstrating that there were two distinct types of instabilities for gravity waves of finite amplitude on deep water. They solved the fully nonlinear equations for water waves, finding that one type is predominantly two-dimensional, relating to all the previously known results for special cases. The other predominantly three-dimensional instability becomes dominant when the wave steepness is large.

The set of equations that McLean et al. solved, working with the velocity potential,  $\varphi$ , was:  $\nabla^2 \varphi = 0$  for  $-\infty < y < \eta(x_1, x_2, t)$ ; and  $\varphi_t + \frac{1}{2}|\nabla\varphi|^2 + gy = 0$ ,  $\eta_t + \nabla\varphi \cdot \eta - \varphi_y = 0$  on  $y = \eta$ . They calculated steady Stokes waves up to  $2a/\lambda = 0.131$  (corresponding to  $ak = 0.412$ ) on the form  $\eta_s = \sum_0^\infty A_n \cos[2n\pi(x_1 - Ct)]$ , where the Fourier coefficients  $A_n$  and the wave speed  $C$  were functions of  $2a/\lambda$ . In the computations  $\lambda$  was put to  $2\pi$  (giving  $k_0 = 1$ ) and  $g = 1$ .  $2a$  denoted the wave height.

They perturbed the steady waves by infinitesimal perturbations  $\eta'$  of the form

$$\eta' = e^{i[p(x_1 - Ct) + qx_2 - \sigma t]} \sum_{-\infty}^{\infty} a_n e^{in(x_1 - Ct)}, \quad (3.1)$$

where the perturbation wavenumbers  $p$  and  $q$  are real numbers. Eq. (3.1) is an eigenvector of the infinitesimal perturbations to the Stokes wave, with  $\sigma$  being the eigenvalue. Instability corresponds to  $Im(\sigma) \neq 0$ , since the perturbation also involves the complex conjugate. The task set by McLean et al. was to determine the eigenvalues,  $\sigma$ . This was done by inserting a truncated version of (3.1), and a corresponding perturbation of the velocity potential,  $\varphi'$ , both including  $2N + 1$  modes, into the full equations. The kinematic and dynamic boundary conditions were satisfied at  $2N + 1$  nodes. The resulting homogeneous system of order  $4N + 2$  was solved as an eigenvalue problem for  $\sigma$  by means of standard methods. McLean et al. used  $N = 20$  for  $2a/\lambda < 0.1$  and  $N = 50$  for the steepest case with  $2a/\lambda = 0.131$ .

In a frame of reference moving with the wave speed,  $C$ , the unperturbed wave, in the limit  $2a/\lambda \rightarrow 0$ , becomes:<sup>21</sup>  $\eta_s = 0$ ,  $\varphi_s = -x_1$ , where  $C$  has been put to unity. In this case, the eigenfunctions and eigenvalues are

$$\eta' = e^{-i\sigma_n t + i[(p+n)x_1 + qx_2]}, \quad (3.2)$$

$$\sigma_n = -k_x \pm |\mathbf{k}|^{\frac{1}{2}}, \quad (3.3)$$

where the latter represents the linear dispersion relation on a unit current (of negative speed), and where  $\mathbf{k} = (k_{x_1}, k_{x_2}) = (p + n, q)$ . Eq. (3.3) gives

$$\sigma_n = -(p + n) \pm [(p + n)^2 + q^2]^{\frac{1}{4}}. \quad (3.4)$$

McLean et al. noted that the  $\sigma$ 's were degenerate in the sense that  $\sigma_n(p, q) = \sigma_{n+1}(p - 1, q)$ . In the case of finite amplitude Stokes waves, the eigenvalues may become complex, meaning instability, if

$$\sigma_{n_1}^{\pm}(p, q) = \sigma_{n_2}^{\pm}(p, q). \quad (3.5)$$

The corresponding eigenvectors have dominant wave vectors  $\mathbf{k}_1 = (p + n_1, q)$  and  $\mathbf{k}_2 = (p + n_2, q)$ . For deep water waves, the solution to (3.5) was divided into two classes:

Class I:

$$\mathbf{k}_1 = (p + m, q), \quad \mathbf{k}_2 = (p - m, q), \quad \sigma_m^+(p, q) = \sigma_{-m}^-(p, q), \quad (3.6)$$

$$[(p + m)^2 + q^2]^{\frac{1}{4}} + [(p - m)^2 + q^2]^{\frac{1}{4}} = 2m, \quad (m \geq 1). \quad (3.7)$$

Class II:

$$\mathbf{k}_1 = (p + m, q), \quad \mathbf{k}_2 = (p - m - 1, q), \quad \sigma_m^+(p, q) = \sigma_{-m-1}^-(p, q), \quad (3.8)$$

$$[(p + m)^2 + q^2]^{\frac{1}{4}} + [(p - m - 1)^2 + q^2]^{\frac{1}{4}} = 2m + 1, \quad (m \geq 1). \quad (3.9)$$

Class I curves are symmetric about  $(p, q) = (0, 0)$ . Class II curves are symmetric about  $(p, q) = (\frac{1}{2}, 0)$ .

The eigenvalues can alternatively be interpreted as resonance of two infinitesimal waves with the carrier wave, giving, in the fixed frame of reference:

$$\omega_1 = -\omega_2 + N\omega_0, \quad \mathbf{k}_1 = \mathbf{k}_2 + N\mathbf{k}_0. \tag{3.10}$$

Here,  $\mathbf{k}_1 = (p' + N, q)$ ,  $\mathbf{k}_2 = (p', q)$  (and  $-\mathbf{k}_2 = (-p', -q)$ ),  $\mathbf{k}_0 = (1, 0)$ , and  $\omega_i = |\mathbf{k}_i|^{\frac{1}{2}}$ . Class I corresponds to  $N$  even,  $m = \frac{1}{2}N$ ,  $p' = p - m$ . Class II corresponds to  $N$  odd,  $m = \frac{1}{2}(N - 1)$ ,  $p' = p - m - 1$ .  $N = 2$  corresponds to 4-wave interaction,  $N = 3$  to 5-wave interaction,  $N = 4$  to 6-wave interaction, and so on. The resonance curves are visualized in figure 1.

For  $p = \frac{1}{2}$  McLean et al. found that  $Re(\sigma) = 0$ , which means that the perturbation wave pattern co-propagates with the Stokes wave. They calculated the regions of nonlinear instability, and moreover, identified the growth rate of the most unstable perturbation (corresponding to maximum of  $|Im(\sigma)|$ ). From McLean et al.,<sup>20</sup> figure 1, we obtain selected values of  $(q, ak, |Im(\sigma)|_{\max})$  (and  $p = \frac{1}{2}$ ):

Table 1. Growth rate of the most unstable perturbation of class II instability; 5-wave interaction.  $p = \frac{1}{2}$ . Extracted from McLean et al.,<sup>20</sup> figure 1.

$q$	$ak$	$ Im(\sigma) _{\max}$
1.65	0.1	$6 \cdot 10^{-4}$
1.53	0.2	$5 \cdot 10^{-3}$
1.25	0.3	$2 \cdot 10^{-2}$
1.16	0.41	$1 \cdot 10^{-1}$

McLean<sup>21</sup> improved the accuracy of the stability calculations. In his table 2 and figure 3, more accurate values of the lateral wavenumber and growth rate were presented. Particularly for  $ak = 0.3$ , a new value of  $q = 1.33$  was obtained, and is used here in the calculations that are discussed below (we use  $q = \frac{4}{3}$ ). It is important to note that improved computations of the stability analysis were required, still. This was particularly true for waves with  $ak$  exceeding 0.412, for which no values were given by

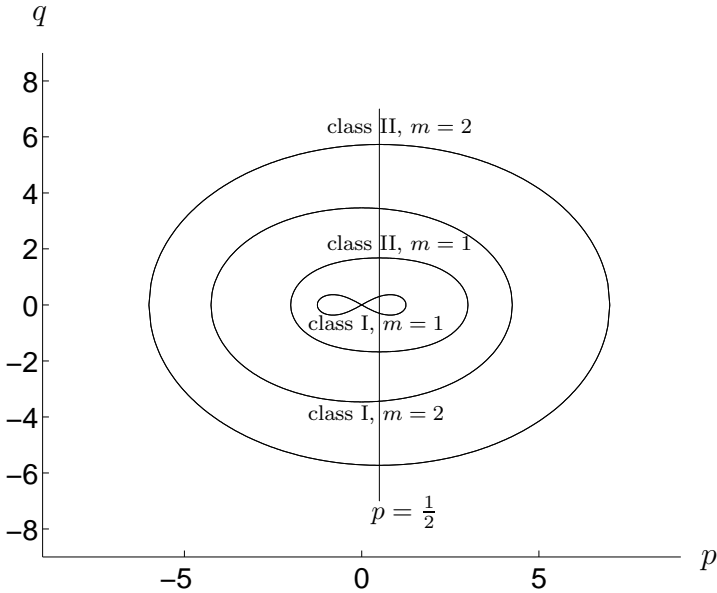


Fig. 1. Plot of resonance curves for  $ak = 0$ . Class I instabilities, eq. (3.7) with  $m = 1$  (inner curve – including points  $(\pm\frac{5}{4}, 0)$ ) and  $m = 2$  (curve including points  $(\pm\frac{17}{4}, 0)$ ). Class II instabilities, eq. (3.9) with  $m = 2$  (outer curve – including points  $(-6, 0)$  and  $(7, 0)$ ) and  $m = 1$  (including points  $(-2, 0)$  and  $(3, 0)$ ). Class II instability curves are symmetric with respect to  $p = \frac{1}{2}$ .

McLean.<sup>21</sup> This was the motivation for the studies by Kharif and Ramanonjarisoa.<sup>23,24</sup>

### 3.2. Computations of the classical horseshoe pattern

The stability analysis of McLean et al.<sup>20</sup> was motivated by the three-dimensional patterns observed experimentally by Su, published in 1982, as mentioned. The waves were also investigated experimentally by Melville,<sup>25</sup> Kusuba and Mitsuyasu<sup>26</sup> and Collard and Caulliez.<sup>27</sup> The experimental observations of the waves are here numerically reproduced in the sense that we compute the growing wave instabilities up to the point of breaking. In the original experiments the Stokes waves had an amplitude corresponding to  $(ak)_0 = 0.33$ . For such steep waves the class II instability is stronger than the class I instability. We here illustrate numerically the growth of the class II instability, where in the computations the class I instability

Table 2. Characteristics of three-dimensional wave patterns. Numerical computations prior to breaking for  $(ak)_0 = 0.2985$  and  $0.33$  compared to experiments of steady pattern by Su,  $(ak)_0 = 0.33$ .  $S_x = \partial\eta/\partial x$ . The numerical waves grow up to breaking during 18 wave periods ( $(ak)_0 = 0.2985$ ) and 11 wave periods ( $(ak)_0 = 0.33$ ).

$(ak)_0$	$\frac{\lambda_2}{\lambda_1}$	$\frac{h_{11}}{h_{12}}$	$\frac{h_{21}}{h_{22}}$	$\frac{h_{11}}{h_{21}}$	$\frac{h_{22}}{h_{11}}$	$\frac{h_{11}+h_{12}}{h_{22}+h_{21}}$	$S_{x,\max}$
Su; 0.33	1.28	1.10	0.88	1.66	0.68	1.49	0.65
Sim, 0.2985	1.28	1.11	0.88	1.56	0.73	1.38	0.66
Sim, 0.33	1.28	1.12	0.85	1.53	0.76	1.33	0.67

is suppressed. Description follows Fructus et al.<sup>28</sup> The waves were also studied numerically by Xue et al.<sup>29</sup> and Fuhrman et al.<sup>30</sup>

Stokes waves with frequency  $\omega_0 = \omega(k_0)$  and wave slope  $(ak)_0$  were computed using the procedure of Fenton.<sup>31</sup> To this wave train, a small perturbation, taking the form

$$\hat{\eta} = \epsilon a_0 \sin((1 + p)k_0 x_1) \cos(qk_0 x_2) \tag{3.11}$$

was superposed. Here,  $\epsilon$  is a small number, making the amplitude of the initial perturbation field a fraction of the Stokes wave field, and  $(1 + p, q)k_0$  denotes the directional wavenumber. Computations performed with  $(ak)_0 = 0.2985$  and  $0.33$ , have perturbation at  $p = \frac{1}{2}$ ,  $q = \frac{4}{3}$  and value of  $\epsilon$  of  $0.05$ .

Four periods of Stokes waves in the longitudinal direction and three periods of perturbation in the lateral direction were resolved by  $128 \times 64$  nodes. The magnitude of the Fourier transform of the perturbation field,  $|\mathcal{F}(\hat{\eta})|$ , visualizes the growth of the modes with wavenumbers  $(\frac{3}{2}, \pm\frac{4}{3})k_0$  up to the point of breaking, see figure 2a. The sum of the wave vectors of the satellites is  $(3, 0)k_0$ . The initial growth rate in the nonlinear calculations is  $0.0194$ , slightly smaller than the analytical value of  $0.021$  computed by perturbation theory, when  $(ak)_0 = 0.2985$ . The frequency spectrum,  $\omega(k_{x_1}, k_{x_2}, t)$ , obtained from the Fourier transformed perturbation field by  $\mathcal{F}(\hat{\eta}) = |\mathcal{F}(\hat{\eta})| \exp(i\chi)$  and  $\omega(k_{x_1}, k_{x_2}, t) = \partial\chi/\partial t$ , shows that  $\omega(\frac{3}{2}k_0, \pm\frac{4}{3}k_0) = \frac{3}{2}\omega_0(1 + \hat{\epsilon})$ , where  $\hat{\epsilon}$  represents a very small variation (caused by interactions with modes of higher wavenumber) around zero and is visualized in figure 2b. Indeed, the figure illustrates that a quintet interaction is evident. The resulting wave field prior to breaking is visualized in figure 4a, and the wave frequency spectrum in figure 4c. The latter exhibits peaks at  $\omega_0$  – the fundamental frequency, and  $n\omega_0$ , ( $n > 1$ ) – the locked components of the Stokes wave. The dominant peaks corresponding

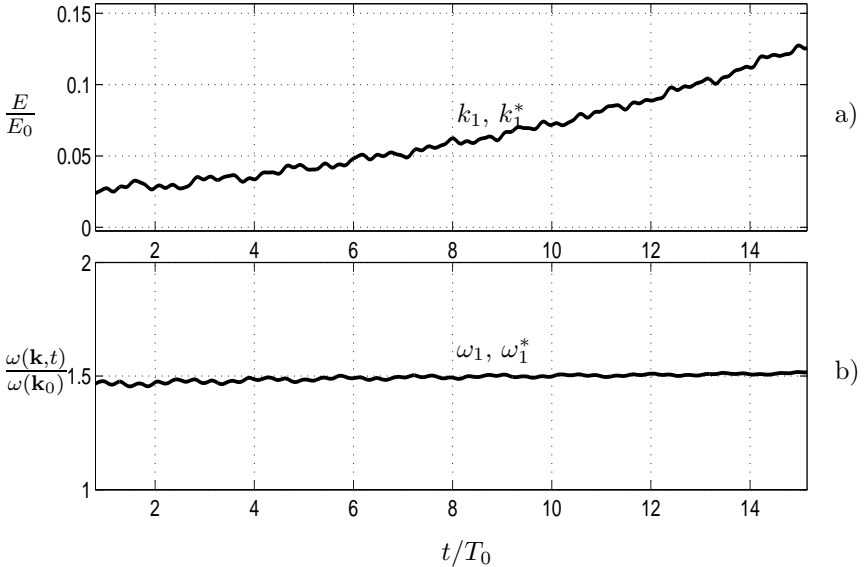


Fig. 2. a) Energy evolution,  $E$ , relative to initial energy,  $E_0 = \frac{1}{2}\rho g a_0^2$ , of the dominant modes:  $\mathbf{k}_1 = (\frac{3}{2}, \frac{4}{3})k_0$  and  $\mathbf{k}_1^* = (\frac{3}{2}, -\frac{4}{3})k_0$ . b) Evolution of frequency. Initial perturbation with  $(p, q) = (\frac{1}{2}, \frac{4}{3})$ .  $(ak)_0 = 0.2985$ ,  $\epsilon = 0.05$ . Adapted from Fructus et al.<sup>28</sup> Reproduced by permission by J. Fluid Mech.

to the satellites is observed at  $\frac{3}{2}\omega_0$ . Higher order motions of the satellites have small peaks at  $\frac{1}{2}\omega_0, \frac{5}{2}\omega_0, \frac{7}{2}\omega_0, \dots$ . The number of time steps in the computation of the waves is indicated in figure 2, 4a,c as visualized in figure 5.

The wave breaking appears in the computations by a rapid growth of the high wavenumbers of the spectrum. The computational wave breaking – when it is independent of the resolution – corresponds to breaking of the physical waves. The computed waves right before breaking resemble the steady state of the three-dimensional wave field in the experiments. Wave characteristics are defined in figure 3. The numerical waves compare very well to the waves in steady state, observed by Su,<sup>19</sup> see table 5. Su termed the pattern by  $L_2$  pattern, since it repeated itself once per two wavelengths of the fundamental train. More generally,  $L_n$  patterns correspond to interactions between satellites  $\mathbf{k}_1 = (1 + 1/n, q)k_0$  and  $\mathbf{k}_2 = (2 - 1/n, -q)k_0$ , meaning that  $p = 1/n$ , where the integer  $n \geq 2$ . The definition can also be used for  $n = 1$  ( $L_1$  pattern) corresponding to  $p = 0$ .

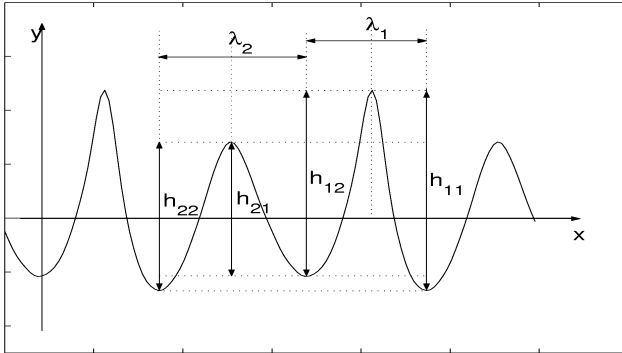


Fig. 3. Definition of Su's geometric parameters.

### 3.3. Oscillating horseshoe pattern. Computations of the experiments by Collard and Caulliez

A new surface wave pattern was experimentally observed by Collard and Caulliez.<sup>27</sup> They performed water wave experiments in a long, relatively wide indoor tank, finding an oscillatory, crescent formed, horse-shoe like pattern, riding on top of long-crested steep Stokes waves with wavenumber  $k_0$ . The crescents of the sideways oscillating pattern were always aligned, both in the longitudinal and transversal directions, see figure 4b for illustration. The wave patterns appeared due to an instability in the form of a quintet resonant interaction: wave satellites had longitudinal wavenumber  $k_0$  and transversal wavenumber  $qk_0$ , and the other wavenumber  $2k_0$  (longitudinal) and  $-qk_0$  (transversal). These summed up to three times the wavenumber of the fundamental Stokes wave. The observed frequencies (in the experiments) were  $1.36\omega_0$ ,  $1.64\omega_0$ , adding up to three times the fundamental frequency,  $\omega_0$  of the Stokes wave, satisfying also a quintet in the frequencies. Along the propagation direction, the pattern repeated itself once per fundamental wave length, and is so an  $L_1$  pattern. The stability analysis above, with  $N = 3$  and  $p = 0$ , supports the observations of the three-dimensional pattern.

This aligned  $L_1$  pattern was numerically evidenced by Skandrani<sup>32</sup> and was also computed by Fuhrman et al.<sup>30</sup> Here we follow Fructus et al.<sup>28</sup> who performed simulations with an initial perturbation corresponding to  $(p, q) = (0, \frac{4}{3})$  and  $\epsilon = 0.05$ , for Stokes waves with  $(ak)_0 = 0.2985$ . The wave field was initially perturbed by  $\mathbf{k}_1 = (1, \frac{4}{3})k_0$ . This perturbation generated a

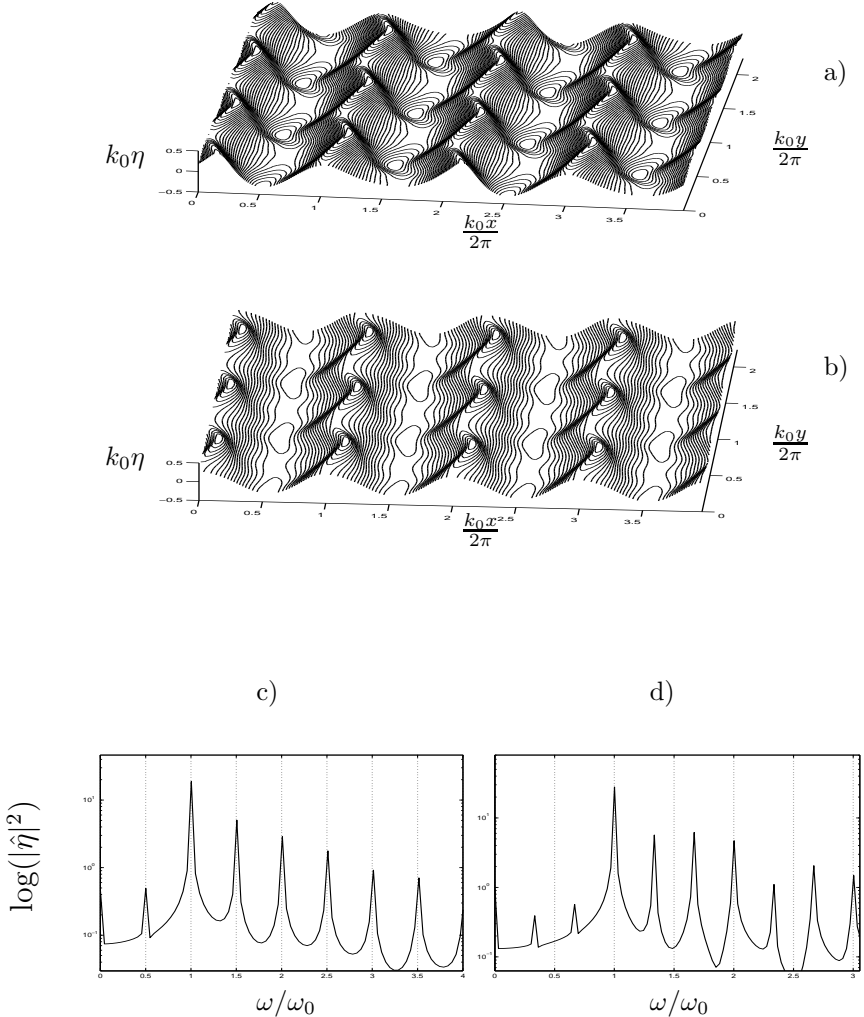


Fig. 4. Three-dimensional wave patterns on Stokes waves with wave slope 0.30 of the fundamental mode. a) Steady (most unstable) horse shoe pattern, observed experimentally by Su in 1982. Snapshot at  $t/T_0 = 16$  ( $T_0$ -wave period). b) Unsteady horse shoe pattern, observed experimentally by Collard and Caulliez in 1999 ( $t/T_0 = 23$ ). c) Wave frequency spectrum corresponding to a). d) Wave frequency spectrum corresponding to b). From Fructus et al.<sup>13</sup>

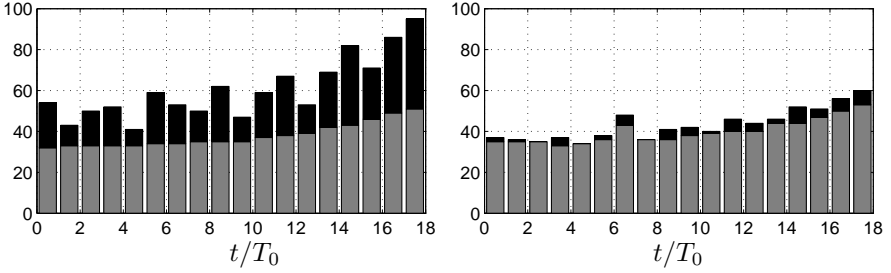


Fig. 5. Number of time steps per wave period for the computation in figure 2. Time integration without (right) and with (left) stabilizing step size control. Number of accepted (grey) and rejected (black) steps per wave period. From Clamond et al.<sup>15</sup>

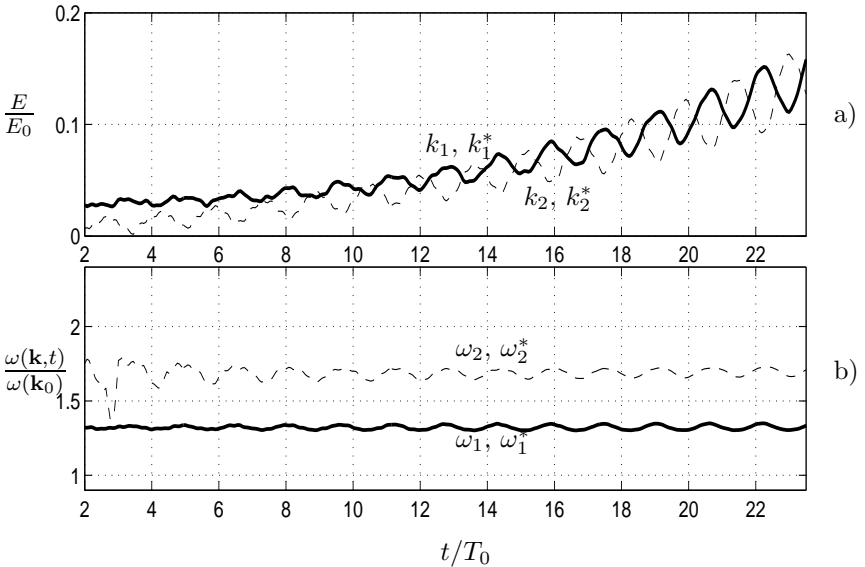


Fig. 6. a) Energy evolution,  $E$ , relative to initial energy,  $E_0 = \frac{1}{2}\rho g a_0^2$ , of the dominant modes:  $\mathbf{k}_1 = (1, \frac{4}{3})k_0$ ,  $\mathbf{k}_1^* = (1, -\frac{4}{3})k_0$ , and  $\mathbf{k}_2 = (2, \frac{4}{3})k_0$ ,  $\mathbf{k}_2^* = (2, -\frac{4}{3})k_0$ . b) Evolution of frequency. Initial perturbation with  $(p, q) = (0, \frac{4}{3})$ .  $(ak)_0 = 0.2985$ ,  $\epsilon = 0.05$ . Adapted from Fructus et al.<sup>28</sup> Reproduced by permission by J. Fluid Mech.

motion with energy at wavenumber  $\mathbf{k}_2^* = (2, -\frac{4}{3})k_0$ . An interaction between the two modes then became evident. The pair of modes with wave vectors  $\mathbf{k}_1 = (1, \frac{4}{3})k_0$ ,  $\mathbf{k}_2^* = (2, -\frac{4}{3})k_0$  satisfied  $\mathbf{k}_1 + \mathbf{k}_2^* = 3\mathbf{k}_0$ . This growth is visualized in figure 6a. The growth is somewhat weaker than for the classical

horseshoe pattern, see figure 2a. The resulting wave field prior to breaking is illustrated in figure 4.

The dominant frequencies of the satellites are visualized in figure 6b. The figure shows that  $\omega(\mathbf{k}_1) + \omega(\mathbf{k}_2^*) = 3\omega_0(1 + \hat{\epsilon})$  where  $\hat{\epsilon}$  represents a small oscillation around zero. The oscillation has period  $\frac{11}{7}$ , approximately, of the fundamental period,  $T_0$ . The dominant frequencies are further illustrated in figure 4d, where peaks in the wave frequency spectrum is observed pair-wise, at  $(n+a)\omega_0$ ,  $(n+1-a)\omega_0$ , for  $n = 0, 1, 2, \dots$ , where  $a = 0.33 \pm 0.02$ . (Note that the value of  $(ak)_0$  is different in the computation and the experiment by Collard and Caulliez, and thus makes a small difference in the value of the peak frequencies of the satellites.) The wave frequencies of the Stokes waves at  $n\omega_0$ ,  $n \geq 1$ , are also present.

The computations by Fructus et al.<sup>28</sup> further showed that the modes  $(\mathbf{k}_1 = (1, \frac{4}{3})k_0, \mathbf{k}_2^* = (2, -\frac{4}{3})k_0)$  and  $(\mathbf{k}_1^* = (1, -\frac{4}{3})k_0, \mathbf{k}_2 = (2, \frac{4}{3})k_0)$  had the same development. A resonant interaction between the two pairs of modes was observed. The triggering mechanism of the waves was investigated, finding that the waves could be generated by parametric resonance due to the wave-maker. This  $L_1$  pattern should be observed in coastal waters where the modulational instability becomes weaker.

### 3.4. Other features of class II instability

#### 3.4.1. Class I instability may restabilize class II instability; $(ak)_0 = 0.10$ .

For moderate  $(ak)_0$  the class II instability may be restabilized by class I instability. In an example, shown in figure 7a, the Stokes wave with  $(ak)_0 = 0.10$  was perturbed by the most unstable modes of the class I and class II instabilities, corresponding to  $p = \frac{1}{6}$  and  $p = \frac{1}{2}$ , with wave vectors  $\mathbf{k}_1 = (\frac{5}{6}, 0)k_0$ ,  $\mathbf{k}_2 = (\frac{7}{6}, 0)k_0$ ,  $\mathbf{k}_3 = (\frac{3}{2}, 1.645)k_0$ ,  $\mathbf{k}_3^* = (\frac{3}{2}, -1.645)k_0$ . The explanation for the restabilization of the class II instability is that the modulational instability moves the very narrow class II instability region slightly (when  $(ak)_0 = 0.1$ ), so that the perturbations at the wave vectors  $\mathbf{k}_3 = (\frac{3}{2}, 1.645)k_0$ ,  $\mathbf{k}_3^* = (\frac{3}{2}, -1.645)k_0$  fall outside the instability region. No breaking was observed in the simulation.

#### 3.4.2. Class II instability may trigger class I instability, leading to breaking; $(ak)_0 \geq 0.10$ .

If the wave field is perturbed by class II instability only, the side-band instability becomes triggered. If  $(ak)_0 \geq 0.10$ , the interaction between

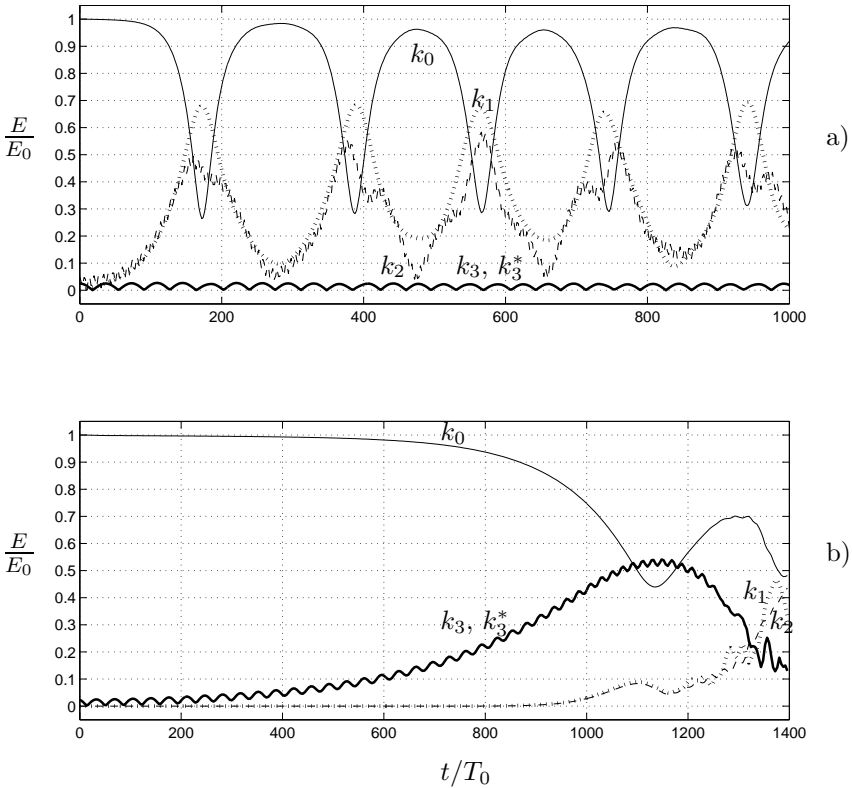


Fig. 7. Energy evolution,  $E$ , relative to initial energy,  $E_0 = \frac{1}{2} \rho g a_0^2$ , of the main modes:  $\mathbf{k}_0 = (1, 0)k_0$ ,  $\mathbf{k}_1 = (\frac{5}{6}, 0)k_0$ ,  $\mathbf{k}_2 = (\frac{7}{6}, 0)k_0$ ,  $\mathbf{k}_3 = (\frac{3}{2}, 1.645)k_0$ ,  $\mathbf{k}_3^* = (\frac{3}{2}, -1.645)k_0$ . Stokes wave with  $(ak)_0 = 0.1$  perturbed initially by a)  $\mathbf{k}_1$ ,  $\mathbf{k}_2$ ,  $\mathbf{k}_3$ ,  $\mathbf{k}_3^*$ , and b)  $\mathbf{k}_3$ ,  $\mathbf{k}_3^*$  only. Adapted from Fructus et al.<sup>28</sup> Reproduced by permission by J. Fluid Mech.

the class II and class I instabilities and the fundamental wave train leads to breaking. An example with the initial unstable perturbation corresponding to the phase-locked crescent-shaped pattern, with wave satellites  $\mathbf{k}_3 = (\frac{3}{2}, 1.645)k_0$ ,  $\mathbf{k}_3^* = (\frac{3}{2}, -1.645)k_0$ , is visualized in figure 7b.

3.4.3. *Class I instability may trigger class II instability, leading to breaking;  $(ak)_0 > 0.12$ .*

Numerical simulations taking into account both class I and class II instabilities show that for moderately steep waves, namely  $(ak)_0 > 0.12$ , their

nonlinear coupling (involving the fundamental of the Stokes wave) results in breaking of the wave when in the initial condition only the modulational instability was considered. This result is in agreement with the experiments conducted by Su and Green.<sup>33</sup>

#### 3.4.4. Class II leading to breaking; $(ak)_0 > 0.17$ .

For steeper waves (in deep water), the strength of class II instability alone is found sufficient to trigger breaking of the wave. It is shown that the nonlinear dynamics of the most unstable class II perturbation lead to breaking when  $(ak)_0 > 0.17$ . For very steep waves (in deep water), with  $(ak)_0 > 0.31$ , class II instability dominates over class I instability, being the primary source of breaking of the waves.

#### 3.4.5. Predominance of class I and class II instabilities.

##### *Recurrence versus breaking. Wave slope thresholds*

Computations show that class I and class II instabilities are equally strong for  $(ak)_0 = 0.314$ , when the water depth is infinite. Below this wave slope the modulational instability is the strongest, while above class II is the strongest. The threshold wave slope becomes reduced when the water depth is finite. For  $kh = 1$ , the value is  $(ak)_0 = 0.1$ , for example. The class II instability exhibits recurrence for  $(ak)_0 < 0.17$  and breaking above this value (when  $h = \infty$ ), while in finite water depth, for  $kh = 1$ , recurrence occurs when  $(ak)_0$  is less than 0.13, approximately. The thresholds are summarized in figure 8. In general, higher order instabilities in the form of 5-, 6- and higher order wave interactions become more important for

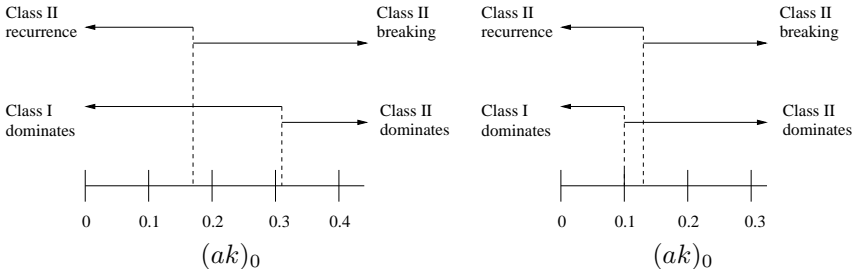


Fig. 8. Predominance of class I and class II instabilities. Recurrence vs. breaking. Infinite depth and  $kh = 1$ . Adapted from Fructus et al.<sup>28</sup> Reproduced by permission by J. Fluid Mech.

shallower water than in deep water, see also Francius and Kharif,<sup>34</sup> Kristiansen et al.<sup>35</sup>

## 4. Computations of Extreme Wave Events

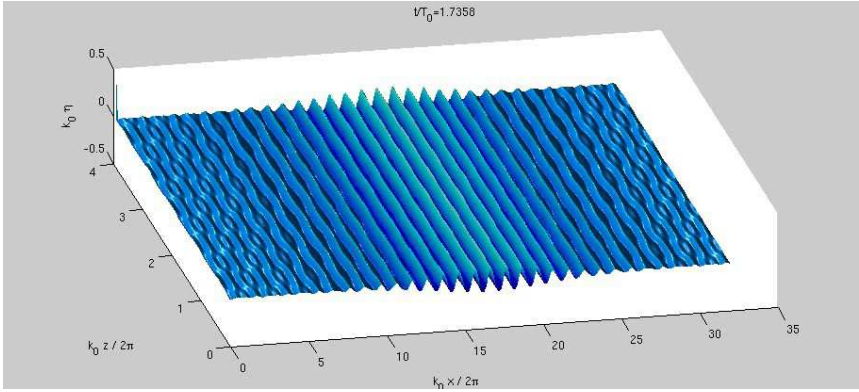
### 4.1. *Effect of sideband instability*

Computations of side-band instability are performed in the following way: A Stokes wave train of initial amplitude  $a_0$  and wavenumber  $k_0$  propagating along the  $x_1$ -direction is multiplied by an amplitude function given by  $\text{sech}[\epsilon_1 \sqrt{2} a_0 k_0^2 x_1]$  where in the present computations  $(a_0 k_0, \epsilon_1) = (0.13, 0.263)$  in figure 9 and  $(0.1, 0.25)$  in figure 10. The values of  $a_0 k_0$  mean that the initial waveslope is relatively moderate, while the values of  $\epsilon_1$  mean that the wavegroup will split into several envelope solitons and form local extreme events during the interaction between the group solitons and the inherent effect of the sideband instability.<sup>36</sup> In the case when  $\epsilon_1 = 1$  the initial condition represents that of an envelope soliton of permanent shape and no large wave events will occur. Figure 9 shows the three-dimensional calculation of the group on a grid that is 32 wavelengths long and four wavelengths wide, where the wavelength is  $\lambda_0 = 2\pi/k_0$ . A resolution of 32 nodes per wavelength in each horizontal direction gives totally  $1.3 \cdot 10^5$  nodes in the calculation where all nonlinear terms are included. The effect of sideband instability is triggered because of the imperfect shape of the amplitude function. The sideband instability moves energy from the fundamental wavenumber to both longer and shorter waves and is visualized in figure 10b. The sideband instability causes a local extreme wave event in the middle of the wave group after a time corresponding to 70 wave periods in figure 9b and 120 wave periods in figure 10a. The largest events are non-breaking. The wave in figure 10 reaches a maximum in  $k\eta_m$  of 0.325 where  $\eta_m$  denotes the maximum elevation above  $y = 0$  and  $k = 2\pi/\lambda$ , where  $\lambda$  is the local trough-to-trough wavelength.

### 4.2. *Events similar to the Camille and Draupner waves*

Very large waves on the ocean have several causes. Here we discuss large waves resulting from nonlinear focusing and linear superposition. Other causes include waves interacting with currents such as the Aghulas current, and wind. Recent reviews of the phenomenon of rogue waves is provided by Kharif and Pelinovsky,<sup>39</sup> see also Grue and Trulsen.<sup>17</sup>

a)



b)

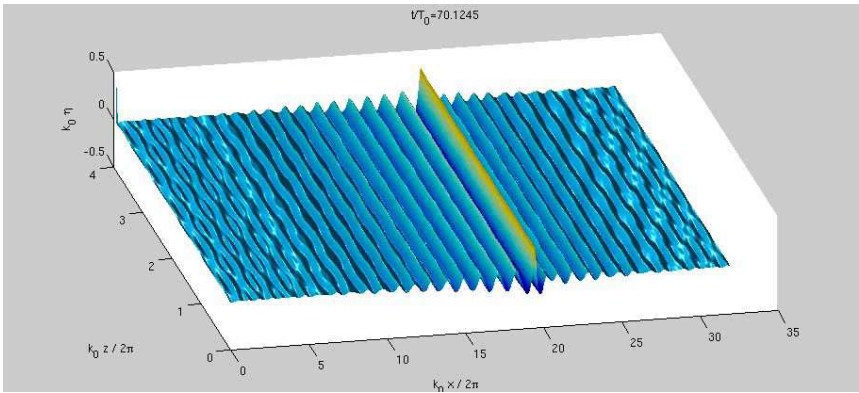


Fig. 9. Formation of an extreme wave event in a modulated long wave group. Initial condition: Stokes wave of amplitude  $a_0$  and wavenumber  $k_0$  multiplied by amplitude function  $\text{sech}[\epsilon_1 \sqrt{2} a_0 k_0^2 x_1]$ , with  $a_0 k_0 = 0.13$ ,  $\epsilon_1 = 0.263$ . a) elevation after 1.73 wave periods, and b) after 70 wave periods.

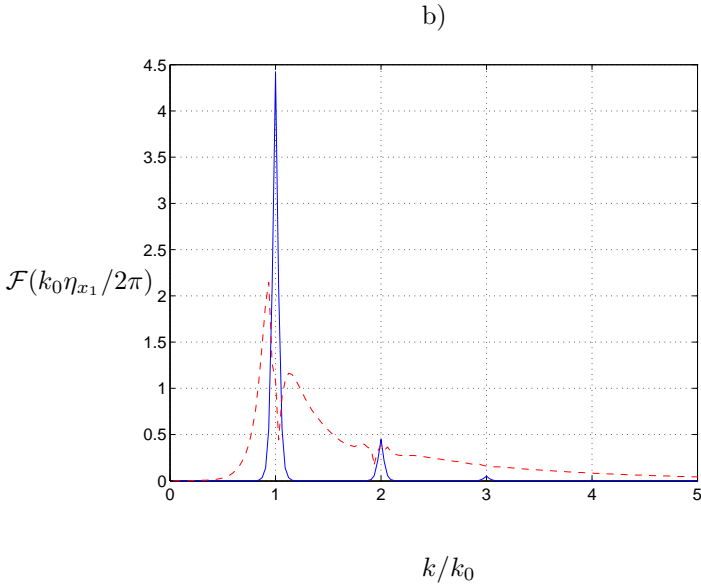
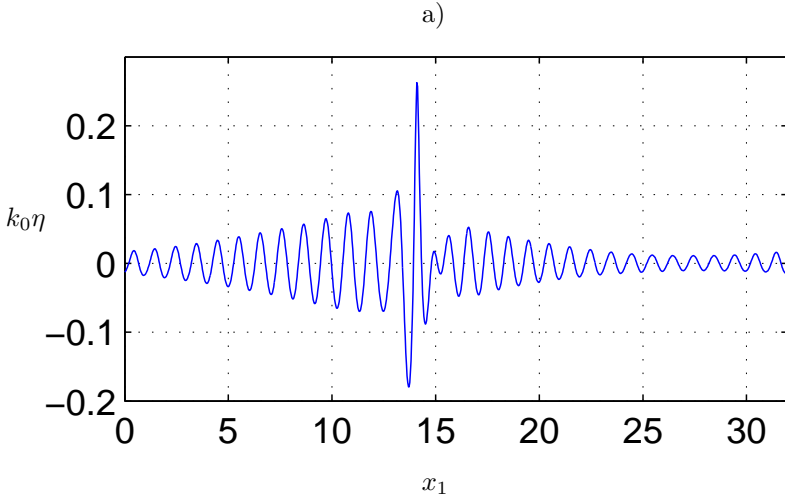


Fig. 10. Same as figure 10, but  $a_0k_0 = 0.1$  and  $\epsilon_1 = 0.25$ . a) elevation after 120 wave periods, and b) wave spectrum,  $\mathcal{F}(\eta_{x_1})$ , at  $t=0$  (solid line) and after 120 wave periods (dashed line).

In order to bridge numerical modeling and physical recordings we use a scaling of the waves, following the documentation provided by laboratory measurements of several large wave events.<sup>40,41</sup> From experimental wave record at a fixed point, the local trough-to-trough period,  $T_{TT}$ , and the maximal elevation above mean water level,  $\eta_m$ , of an individual steep wave event were obtained. The local wavenumber,  $k$ , an estimate of the wave slope,  $\epsilon$ , and a reference velocity were defined by, respectively,

$$\omega^2/gk = 1 + \epsilon^2, \quad k\eta_m = \epsilon + \frac{1}{2}\epsilon^2 + \frac{1}{2}\epsilon^3, \quad \epsilon\sqrt{g/k}, \quad (4.1)$$

where  $\omega = 2\pi/T_{TT}$ .

We compute wave events that match the very large Camille and Draupner waves measured in the field using the scaling (4.1). These very large events at sea are much referred to because of their unique documentation. The time records of the waves provide unique references for how very large ocean waves look like, and for how large and steep they may become. The time series of the Camille and Draupner waves may be found in Ochi<sup>37</sup> figure 8, p. 218, and Trulsen,<sup>38</sup> respectively. Estimates using the scaling (4.1) gives  $\epsilon \simeq 0.38$ ,  $k\eta_m \simeq 0.49$  for the Camille wave and  $\epsilon \simeq 0.39$ ,  $k\eta_m \simeq 0.49$  for the Draupner wave, and is about 50 per cent above the computations shown in figures 9–10. The non-dimensional wave phase velocity estimated from (4.1) becomes  $[\omega/k]/[\epsilon\sqrt{g/k}] = \sqrt{1 + \epsilon^2}/\epsilon \simeq 2.75$ , and  $u/[\omega/k] \simeq 0.67$ , for the Draupner wave.

#### 4.2.1. Non-breaking wave events

Large waves developing from a perturbed Stokes wave train moving in a periodic five wavelength's long numerical tank are computed. While these simulations are classical and follow earlier studies<sup>42,43</sup> less emphasis has been given to the wave kinematics, however. The Stokes waves with initial wave slope  $a_0k_0$  are perturbed by

$$\epsilon_0 a_0 \cos\left(\frac{n+m}{n}k_0 x_1\right) + \epsilon_0 a_0 \cos\left(\frac{n-m}{n}k_0 x_1\right) \quad (4.2)$$

where the value of  $\epsilon_0$  is put to 0.1, and  $n = 5$ ,  $m = 1$ . The latter means that perturbations are initiated at wavenumbers 0.8 and 1.2 times  $k_0$ . The first simulation with  $a_0k_0 = 0.11$  develops recurrence and does not break.<sup>43</sup> Large events develop, as illustrated in figure 11a, with trough-to-trough wavenumber, maximal elevation and value of  $\epsilon$  extracted using (4.1), giving that  $\epsilon = 0.32$ ,  $k\eta_m = 0.39$ ,  $u/c$  up to 0.45 after 83 wave periods (the largest

event), while  $\epsilon = 0.29$ ,  $k\eta_m = 0.34$ ,  $u/c$  up to 0.39 after 83.5 wave periods, and  $\epsilon = 0.23$  after 84.5 wave periods.

Baldock et al.<sup>44</sup> developed non-breaking events in physical wave tank using linear focusing technique (superposition), measuring both surface elevation and wave induced velocities using Laser Doppler Anemometry. A recalculation using (4.1) gives  $\epsilon = 0.29$  and  $k\eta_m = 0.34$  for their largest wave event. We have evaluated the wave induced velocity profile below crest of the large events shown in figures 11a and c. The velocity profiles for  $\epsilon = 0.29$ , divided by the reference velocity  $\epsilon\sqrt{g/k}$ , are plotted in figure 12a together with experimental data, also with  $\epsilon = 0.29$ . The figure illustrates that the non-dimensional velocity profile below crest is almost the same for the three large wave events, even though they have rather different origin, being, in the theoretical computations, the result of nonlinear focusing in a short wave group (figure 11a) and long wave group (figure 11c), and linear superposition in experiment.<sup>44</sup> We may conclude that gravity waves with  $\epsilon < 0.32$ ,  $k\eta_m < 0.39$  and  $u/c < 0.45$  are non-breaking, while waves with  $\epsilon > 0.32$ ,  $k\eta_m > 0.39$  and  $u/c > 0.45$  develop breaking.

#### 4.2.2. *Very large wave events; waves developing breaking*

In the next set of simulations we put  $a_0k_0 = 0.1125$  in the initial perturbation (4.2) leading to breaking.<sup>43</sup> Resulting waves exhibit  $\epsilon = 0.32$ ,  $k\eta_m = 0.39$  after 82.9 wave periods;  $\epsilon = 0.36$ ,  $k\eta_m = 0.45$  after 85.2 periods; and  $\epsilon = 0.38$ ,  $k\eta_m = 0.49$  after 85.4 periods (figure 11b). The numerical waves develop steepening towards breaking for subsequent time and the computations are stopped. Computational velocity profile below crest for the largest wave with  $\epsilon = 0.38$  compares well with measured velocity profiles of the six largest among 122 wave events<sup>40,41</sup> with value of  $\epsilon$  in the range 0.40–0.46, obtained using Particle Image Velocimetry (PIV), see figure 12b. There is a strong match between computation and experiment and is true even though the large computational wave was produced by nonlinear focusing resulting from side band instability, while the experimental waves were produced by linear superposition.

Computational velocity vectors along the free surface obtained for the two largest waves with  $\epsilon = 0.36$ , 0.38 (figure 13a) are compared to experimental velocity vectors in a non-overturning event with  $\epsilon = 0.40$  (figure 13b) and a moderately overturning event with  $\epsilon = 0.41$  (figure 13c). The computational and experimental velocity vectors have the following main features: the maximal horizontal velocities have non-dimensional values up

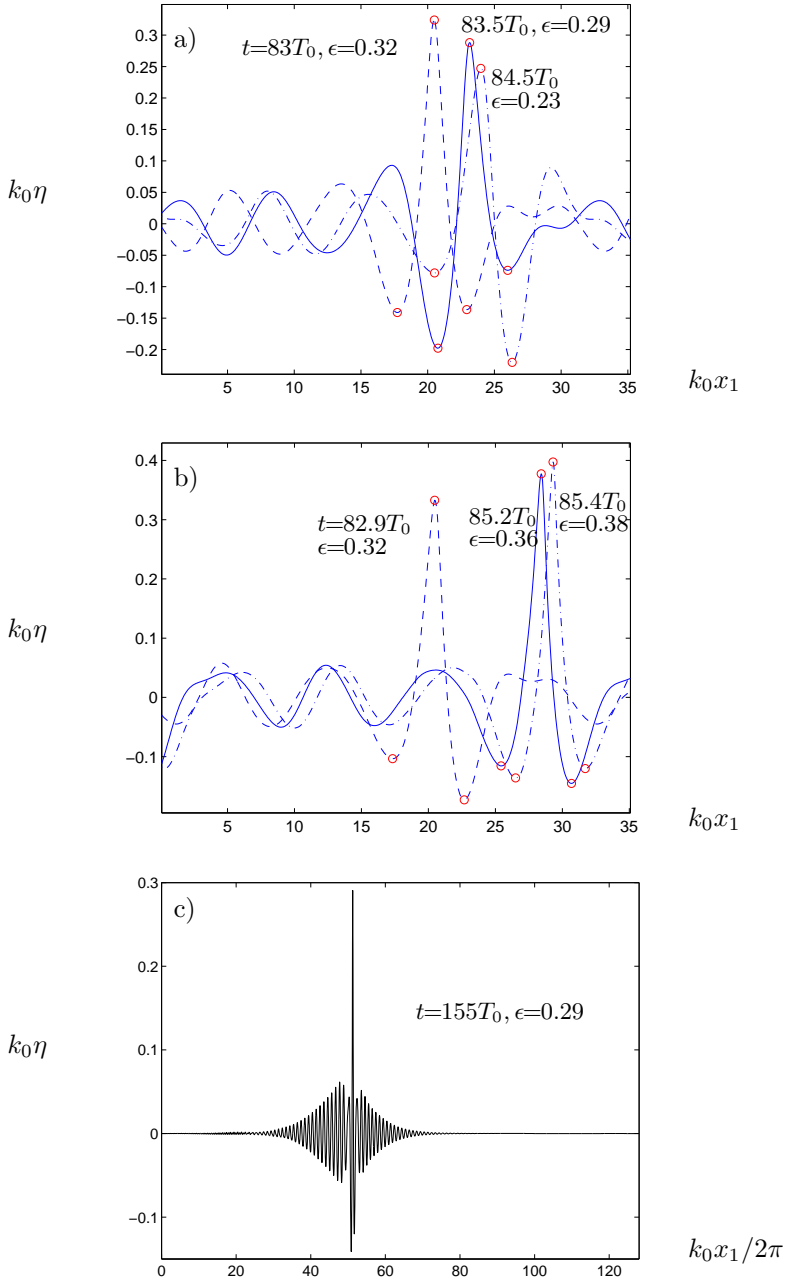


Fig. 11. Large wave events in periodic wave tank. a) Non-Breaking case. b) Breaking case. c) Non-Breaking large wave event during the split-up of a long wave group.<sup>36</sup>

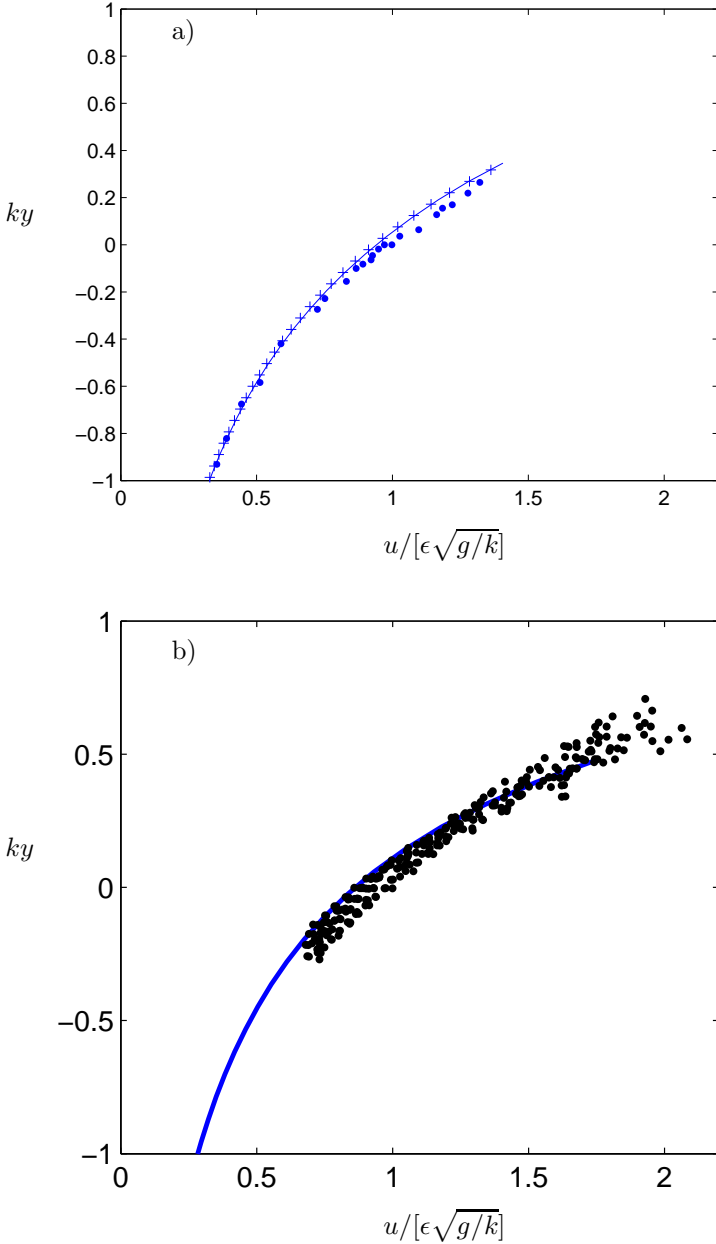


Fig. 12. Horizontal velocity profile below crest scaled by  $\epsilon\sqrt{g/k}$ , as defined in eq. (4.1). a) Velocity profile for the wave in figure 11a at  $t=83.5T_0$  and  $\epsilon = 0.29$  (solid line), for the wave in figure 11c and  $\epsilon = 0.29$  (+ + +), experiments by Baldock et al.<sup>44</sup> (dots). b) Velocity profile for the wave in figure 11b at  $t=85.4T_0$  and  $\epsilon = 0.38$  (solid line) and data from experiments<sup>40,41</sup> and  $\epsilon = 0.40 - 46$  (dots).

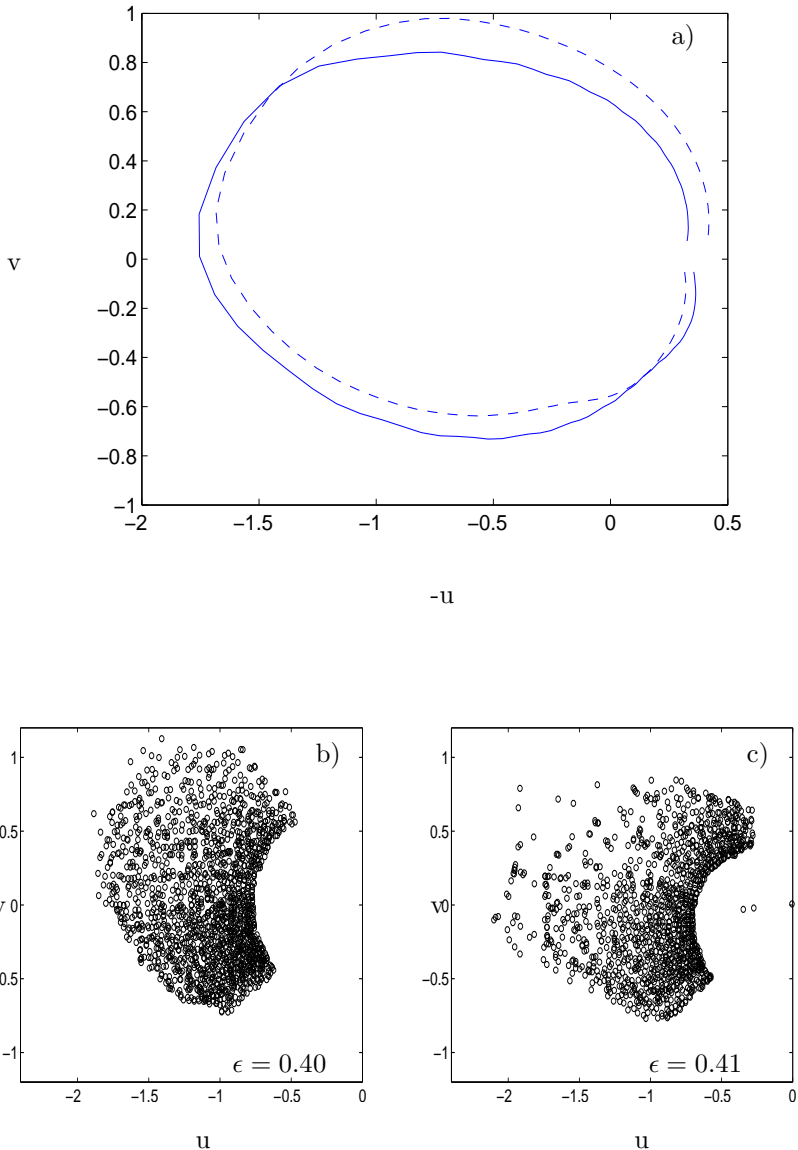


Fig. 13. Non-dimensional velocity plane vectors  $(u, v) = (u, v)/\epsilon\sqrt{g/k}$ . a) Computed velocity vectors along the surface of the wave, with  $\epsilon = 0.36$  (dashed line) and  $\epsilon = 0.38$  (solid line). b)–c): Experimental velocity plane vectors with  $\epsilon = 0.40$  (non-breaking) and  $\epsilon = 0.41$  (breaking).<sup>41</sup>

to, about, 1.75 for  $\epsilon = 0.38$ ; 1.85 for  $\epsilon = 0.40$ ; and 2 for  $\epsilon = 0.41$  (overturning). (The real velocity is obtained multiplying by  $\epsilon\sqrt{g/k}$ .) The velocity plot is asymmetric with larger velocities in the front part of the wave than in the rear. When the wave is about to break, the horizontal velocities exhibit increase, while the vertical velocities become reduced. The results shown here, with  $\epsilon$  in the range about 0.38–0.4, and  $k\eta_m$  up to about 0.49, document that the Camille and Draupner waves eventually developed into breaking.

The non-dimensional wave phase velocity is estimated using (4.1) giving  $[\omega/k]/[\epsilon\sqrt{g/k}] = \sqrt{1 + \epsilon^2}/\epsilon$ . The numerical values of this quantity are 2.8 for  $\epsilon = 0.38$  (figure 13a); 2.6 for  $\epsilon = 0.40$  (figure 13b); and 2.5 for  $\epsilon = 0.41$  (figure 13c). It can be concluded that the fluid velocity is significantly smaller than the wave phase velocity in the examples discussed.

## 5. Generalization to Variable Bottom Topography

We now extend the fully nonlinear and fully dispersive method accounting for a sea floor that is varying in both space and time, following derivations by Fructus and Grue.<sup>45</sup> The sea floor is represented by the function  $y = -h + \delta(\mathbf{x}, t)$  where  $h$  is constant. A scaled normal velocity of the moving sea bottom is introduced by  $V_b = \partial\delta/\partial t = \partial\phi/\partial n\sqrt{1 + |\nabla\delta|^2}$  where the normal vector at the sea floor points into the fluid.

The prognostic equation (2.6) and the time integration procedures discussed below (2.6) are used to integrate  $\eta$  and  $\tilde{\phi}$  forward in time once the (scaled) normal velocity at the free surface,  $V$ , and the velocity potential at the bottom topography,  $\phi_b$  are found, see below. At each time step  $V$  has to be evaluated, given  $\eta$ ,  $\tilde{\phi}$  and the shape and motion of the sea bottom. This implies the solution of a coupled set of integral equations for  $V$  and  $\phi_b$ .

### 5.1. Laplace equation solver. Field point on free surface

Solution of the Laplace equation is obtained by applying Green's theorem to the velocity potential  $\phi$  and a suitable source Green function. For an evaluation point that is on the free surface we obtain

$$\int_{S+B} \left( \frac{1}{r} + \frac{1}{r_B} \right) \frac{\partial\phi'}{\partial n_1'} dS' = 2\pi\phi + \int_{S+B} \phi' \frac{\partial}{\partial n_1'} \left( \frac{1}{r} + \frac{1}{r_B} \right) dS', \quad (5.1)$$

where  $r^2 = R^2 + (y' - y)^2$ ,  $r_B^2 = R^2 + (y' + y + 2h)^2$ ,  $\mathbf{R} = \mathbf{x}' - \mathbf{x}$ , and  $R = |\mathbf{x}' - \mathbf{x}|$ . Further,  $S$  denotes the instantaneous free surface and  $B$

the instantaneous sea bottom. The normal  $n_1$  is pointing out of the fluid ( $n = n_1$  at the free surface, and  $n = -n_1$  at the sea-floor). We introduce  $dS = \sqrt{1 + |\nabla\eta|^2}d\mathbf{x}$  at the free surface  $S$  and  $dS = \sqrt{1 + |\nabla\delta|^2}d\mathbf{x}$  at the sea bottom  $B$ . For notation we use (as before)  $\eta' = \eta(\mathbf{x}', t)$ ,  $\eta = \eta(\mathbf{x}, t)$ ,  $\delta' = \delta(\mathbf{x}', t)$ ,  $\delta = \delta(\mathbf{x}, t)$  and so on. The integral equation may be expressed on the form

$$\int_S \left( \frac{1}{r} + \frac{1}{r_B} \right) V' d\mathbf{x}' = 2\pi\tilde{\phi} + \int_S \tilde{\phi}' \frac{\partial}{\partial n'} \left( \frac{1}{r} + \frac{1}{r_B} \right) \sqrt{1 + |\nabla'\eta'|^2} d\mathbf{x}' + \int_B \left( \frac{1}{r} + \frac{1}{r_B} \right) V_b' d\mathbf{x}' - \int_B \phi_b' \frac{\partial}{\partial n'} \left( \frac{1}{r} + \frac{1}{r_B} \right) \sqrt{1 + |\nabla'\delta'|^2} d\mathbf{x}', \quad (5.2)$$

which is valid on the free surface at  $y = \eta(\mathbf{x}, t)$ . We evaluate the terms

$$\int_B \left( \frac{1}{r} + \frac{1}{r_B} \right) V_b' d\mathbf{x}', \quad - \int_B \phi_b' \frac{\partial}{\partial n'} \left( \frac{1}{r} + \frac{1}{r_B} \right) \sqrt{1 + |\nabla'\delta'|^2} d\mathbf{x}'. \quad (5.3)$$

We note that

$$\frac{1}{r} + \frac{1}{r_B} = \frac{2}{R_2} + 2\eta \frac{\partial}{\partial h} \frac{1}{R_2} + (\delta'^2 + \eta^2) \frac{\partial^2}{\partial h^2} \frac{1}{R_2} + \frac{1}{R_1}, \quad (5.4)$$

where  $R_2^2 = R^2 + h^2$  (and  $R = |\mathbf{x}' - \mathbf{x}|$ ). The first three terms on the right of (5.4) are the leading terms of the sources on the left of the equation. The remaining part is defined by the difference, i.e.

$$\frac{1}{R_1} = \frac{1}{r} + \frac{1}{r_B} - \frac{2}{R_2} - 2\eta \frac{\partial}{\partial h} \frac{1}{R_2} - (\delta'^2 + \eta^2) \frac{\partial^2}{\partial h^2} \frac{1}{R_2},$$

and is a small quantity, decaying rapidly with  $R$ . Now, we use that

$$\frac{\partial^n}{\partial h^n} \frac{1}{R_2} = \mathcal{F}^{-1} \left\{ \frac{2\pi(-k)^n}{k} e^{-i\mathbf{k}\cdot\mathbf{x}' - kh} \right\}. \quad (5.5)$$

( $\mathcal{F}^{-1}$  denotes inverse Fourier transform.) We evaluate the integral, giving

$$\int_B \left( \frac{1}{r} + \frac{1}{r_B} \right) V_b' d\mathbf{x}' = \mathcal{F}^{-1} \{ 4\pi e^{-kh} \mathcal{F}(V_b) / k \} - \eta \mathcal{F}^{-1} \{ 4\pi e^{-kh} \mathcal{F}(V_b) \} + \mathcal{F}^{-1} \{ 2\pi k e^{-kh} \mathcal{F}(\delta^2 V_b) \} + \eta^2 \mathcal{F}^{-1} \{ 2\pi k e^{-kh} \mathcal{F}(V_b) \} + \int_B \left( \frac{1}{R_1} \right) V_b' d\mathbf{x}'. \quad (5.6)$$

To evaluate the second integral in (5.3) we first note that

$$\sqrt{1 + |\nabla'\delta'|^2} \frac{\partial}{\partial n'} \left( \frac{1}{r} + \frac{1}{r_B} \right) = \frac{\mathbf{R} \cdot \nabla'\delta' - y' + y}{r^3} + \frac{\mathbf{R} \cdot \nabla'\delta' - y' - y - 2h}{r_B^3},$$

where  $y' = -h + \delta'$  on the sea floor and  $y = \eta$  on the sea surface. The r.h.s. of the equation may be developed by

$$\sqrt{1 + |\nabla' \delta'|^2} \frac{\partial}{\partial n'} \left( \frac{1}{r} + \frac{1}{r_B} \right) = -2\nabla' \cdot \left( \delta' \nabla' \frac{1}{R_2} \right) - 2\eta \nabla' \cdot \left( \delta' \nabla' \frac{\partial}{\partial h} \frac{1}{R_2} \right) + \frac{1}{\mathcal{R}_2},$$

where the two first terms on the right give the leading contributions to the left hand side and  $1/\mathcal{R}_2$  is a small remainder. We obtain for the integral

$$\begin{aligned} & - \int_B \phi_b' \frac{\partial}{\partial n} \left( \frac{1}{r} + \frac{1}{r_B} \right) \sqrt{1 + |\nabla' \delta'|^2} \, d\mathbf{x}' = \mathcal{F}^{-1} \{ 4\pi i e^{-kh} (\mathbf{k}/k) \cdot \mathcal{F}(\delta \nabla \phi_b) \} \\ & - \eta \mathcal{F}^{-1} \{ 4\pi i e^{-kh} \mathbf{k} \cdot \mathcal{F}(\delta \nabla \phi_b) \} - \int_B \left( \frac{1}{\mathcal{R}_2} \right) \phi_b' \, d\mathbf{x}'. \end{aligned} \tag{5.7}$$

Adding contributions (5.6) and (5.7) we obtain

$$\begin{aligned} & \mathcal{F}^{-1} \left\{ \frac{1 + e_h}{k} [\mathcal{F}(V) + i\mathbf{k} \cdot \mathcal{F}(\eta \nabla \tilde{\phi})] \right\} = \mathcal{F}^{-1} \left\{ (1 - e_h) \mathcal{F}(\tilde{\phi} - \eta V^{(1)}) \right\} \\ & + \mathcal{F}^{-1} \{ e_h \mathcal{F}(\eta(V - V^{(1)})) \} + T(\tilde{\phi}) + T_1(\tilde{\phi}) + N(V) + N_1(V) \\ & + \eta \mathcal{F}^{-1} (e_h \mathcal{F}(V - V^{(1)})) + \mathcal{F}^{-1} \left\{ \frac{2\sqrt{e_h} \mathcal{F}(V_b)}{k} \right\} \\ & - \eta \mathcal{F}^{-1} \{ 2\sqrt{e_h} \mathcal{F}(V_b) \} + \mathcal{F}^{-1} \{ k\sqrt{e_h} \mathcal{F}(\delta^2 V_b) \} + \eta^2 \mathcal{F}^{-1} \{ k\sqrt{e_h} \mathcal{F}(V_b) \} \\ & + \mathcal{F}^{-1} \left\{ \frac{i\mathbf{k}}{k} \cdot 2\sqrt{e_h} \mathcal{F}(\delta \nabla \phi_b) \right\} - \eta \mathcal{F}^{-1} \{ 2i\sqrt{e_h} \mathbf{k} \cdot \mathcal{F}(\delta \nabla \phi_b) \} \\ & + \int_B \left( \frac{1}{\mathcal{R}_1} \right) V_b' \, d\mathbf{x}' - \int_B \left( \frac{1}{\mathcal{R}_2} \right) \phi_b' \, d\mathbf{x}', \end{aligned} \tag{5.8}$$

where  $e_h = e^{-2kh}$  and  $V^{(1)}$  is given in eq. (5.19) below. The functions  $T(\tilde{\phi})$ ,  $N(V)$ ,  $N_1(V)$  and  $T_1(\tilde{\phi})$  are the same as in eq. (2.17). In (5.8) we have divided by a factor of  $2\pi$ .

**5.2. Field point on bottom surface**

An additional equation for the velocity potential  $\phi_b$  at the uneven sea bottom is required in order to solve (5.2), and is obtained by the application of Green’s theorem as well. In the case when the field point is on the sea bottom, we employ  $1/r + 1/r_C$  where  $r^2 = R^2 + (y' - y)^2$ , and  $r_C^2 = R^2 + (y' + y)^2$  is the image with respect with  $y = 0$ . The resulting equation becomes

$$\begin{aligned} 2\pi\phi_b &= \int_S \left( \frac{1}{r} + \frac{1}{r_C} \right) V' \, d\mathbf{x}' - \int_S \tilde{\phi}' \frac{\partial}{\partial n} \left( \frac{1}{r} + \frac{1}{r_C} \right) \sqrt{1 + |\nabla' \eta'|^2} \, d\mathbf{x}' \\ & - \int_B \left( \frac{1}{r} + \frac{1}{r_C} \right) V_b' \, d\mathbf{x}' + \int_B \phi_b' \frac{\partial}{\partial n} \left( \frac{1}{r} + \frac{1}{r_C} \right) \sqrt{1 + |\nabla' \delta'|^2} \, d\mathbf{x}', \end{aligned} \tag{5.9}$$

and is valid for  $y = -h + \delta(\mathbf{x}, t)$ . For the integration over  $B$  we note that

$$\frac{1}{r} + \frac{1}{r_c} = \frac{1}{R} + \frac{1}{R_1} - (\delta' + \delta) \frac{\partial}{\partial(2h)} \frac{1}{R_1} + \frac{1}{\mathcal{R}_3}, \quad (5.10)$$

where the first three terms on the right capture the leading behaviour of the function on the left,  $R_1^2 = R^2 + (2h)^2$ , and  $1/\mathcal{R}_3$  is a small remainder. Further,

$$\begin{aligned} & \sqrt{1 + |\nabla' \delta'|^2} \frac{\partial}{\partial n'} \left( \frac{1}{r} + \frac{1}{r_c} \right) \\ &= -\nabla' \cdot \left( (\delta' - \delta) \nabla' \frac{1}{R} \right) - \nabla' \cdot \left( (\delta' + \delta) \nabla' \frac{1}{R_1} \right) - \frac{\partial}{\partial(2h)} \frac{1}{R_1} + \frac{1}{\mathcal{R}_4}. \end{aligned} \quad (5.11)$$

For the integration over  $S$  we obtain

$$\frac{1}{r} + \frac{1}{r_c} = \frac{2}{R_2} - 2\delta \frac{\partial}{\partial h} \frac{1}{R_2} + \frac{1}{\mathcal{R}_5}, \quad (5.12)$$

$$\sqrt{1 + |\nabla' \eta'|^2} \frac{\partial}{\partial n'} \left( \frac{1}{r} + \frac{1}{r_c} \right) = -\nabla' \cdot \left( 2\eta' \nabla' \frac{1}{R_2} \right) + \frac{1}{\mathcal{R}_6}. \quad (5.13)$$

Now, using (5.5) and

$$\frac{1}{R} = \mathcal{F}^{-1} \left\{ \frac{2\pi}{k} e^{-i\mathbf{k} \cdot \mathbf{x}'} \right\}, \quad \frac{1}{R_1} = \mathcal{F}^{-1} \left\{ \frac{2\pi}{k} e^{-i\mathbf{k} \cdot \mathbf{x}' - 2kh} \right\}, \quad (5.14)$$

we may evaluate the integrals in (5.9). The equation becomes:

$$\begin{aligned} & 2\pi\phi_b = 2\pi\mathcal{F}^{-1}(\mathcal{A}) \\ & + \int_S \left( \frac{1}{\mathcal{R}_5} \right) V d\mathbf{x}' - \int_B \left( \frac{1}{\mathcal{R}_3} \right) V_b d\mathbf{x}' - \int_S \left( \frac{1}{\mathcal{R}_6} \right) \tilde{\phi} d\mathbf{x}' + \int_B \left( \frac{1}{\mathcal{R}_4} \right) V d\mathbf{x}' \end{aligned} \quad (5.15)$$

where

$$\begin{aligned} \mathcal{A} &= \frac{2\sqrt{e_h}\mathcal{F}(V)}{k} + 2\delta\sqrt{e_h}\mathcal{F}(V) - \frac{(1 + e_h)\mathcal{F}(V_b)}{k} - \delta e_h\mathcal{F}(V_b) - e_h\mathcal{F}(\delta V_b) \\ &+ \frac{2i\mathbf{k}}{k} \cdot \sqrt{e_h}\mathcal{F}(\eta\nabla\tilde{\phi}) + e_h\mathcal{F}(\phi_b) - \delta(1 - e_h)k\mathcal{F}(\phi_b) - \frac{i\mathbf{k}}{k} \cdot (1 + e_h)\mathcal{F}(\delta\nabla\phi_b). \end{aligned} \quad (5.16)$$

By taking the Fourier transform on both sides of (5.15) we obtain

$$\begin{aligned} \mathcal{F}(\phi_b) &= \mathcal{F}(\phi_b^{(1)}) + \mathcal{F}(\delta V_b) + \frac{\mathbf{ik} \cdot \mathcal{F}(\eta \nabla \tilde{\phi})}{k \sinh kh} - \frac{\mathbf{ik} \cdot \mathcal{F}(\delta \nabla \phi_b)}{k \tanh kh} \\ &- \frac{1}{1 - e_h} \mathcal{F}(\delta \mathcal{F}^{-1}\{k(1 - e_h)[\mathcal{F}(\phi_b) - \mathcal{F}(\phi_b^{(1)})]\}) \\ &+ \int_S \left(\frac{1}{\mathcal{R}_5}\right) V d\mathbf{x}' - \int_B \left(\frac{1}{\mathcal{R}_3}\right) V_b d\mathbf{x}' - \int_S \left(\frac{1}{\mathcal{R}_6}\right) \tilde{\phi} d\mathbf{x}' + \int_B \left(\frac{1}{\mathcal{R}_4}\right) V d\mathbf{x}', \end{aligned} \tag{5.17}$$

where

$$\mathcal{F}(\phi_b^{(1)}) = \frac{\mathcal{F}(V)}{k \sinh kh} - \frac{\mathcal{F}(V_b)}{k \tanh kh} = \frac{\mathcal{F}(\tilde{\phi})}{\cosh kh} - \frac{\tanh kh \mathcal{F}(V_b)}{k}. \tag{5.18}$$

Similarly,

$$\mathcal{F}(V^{(1)}) = k \tanh hk \mathcal{F}(\tilde{\phi}) + \frac{\mathcal{F}(V_b)}{\cosh hk}. \tag{5.19}$$

The linear approximation (5.18)–(5.19) is a variant of previous solutions.<sup>46</sup>

### 5.3. Successive approximations

Equations (5.18)–(5.19) represent a first step in a series of successive approximations to the full solution. An improved approximation to the non-linear wave field is obtained by keeping terms that are linear in  $\eta$ ,  $\eta'$ ,  $\delta$  and  $\delta'$ , giving

$$\mathcal{F}(V^{(2)}) = \mathcal{F}(V^{(1)}) - k \tanh hk \mathcal{F}(\eta V^{(1)}) + \mathbf{ik} \cdot \mathcal{F}\{\eta \nabla \tilde{\phi}\} + \frac{\mathbf{ik} \cdot \mathcal{F}\{\delta \nabla \phi_b^{(1)}\}}{\cosh hk}, \tag{5.20}$$

$$\mathcal{F}(\phi_b^{(2)}) = \mathcal{F}(\phi_b^{(1)}) - \frac{\mathcal{F}(\eta V^{(1)})}{\cosh hk} - \frac{i \tanh hk}{h} \mathbf{k} \cdot \mathcal{F}\{\delta \nabla \phi_b^{(1)}\} + \mathcal{F}(\delta V_b), \tag{5.21}$$

where  $\phi_b^{(1)}$  and  $V^{(1)}$  are obtained from (5.18)–(5.19). By performing another analytical iteration, keeping terms in the kernels of the integral

equations that are quadratic in  $\eta$ ,  $\eta'$ ,  $\delta$  and  $\delta'$ , we obtain

$$\begin{aligned} \mathcal{F}(V^{(3)}) &= \mathcal{F}(V^{(2)}) - [k \tanh hk \mathcal{F}(\eta(V^{(2)} - V^{(1)})) - \frac{k^2}{2} \mathcal{F}(\eta^2 V^{(1)})] \\ &+ \frac{k}{1 + e_h} \left\{ \mathcal{F}(\eta \mathcal{F}^{-1}[-i\mathbf{k} \cdot \mathcal{F}\{\eta \nabla \tilde{\phi}\}]) + i \frac{e_h}{2} \mathbf{k} \cdot \mathcal{F}\{\eta^2 \nabla \tilde{\phi}\} - \mathcal{F}\{\eta^2 \mathcal{F}^{-1}[\frac{k^2}{2} \tilde{\phi}]\} \right\} \\ &+ \frac{k}{1 + e_h} \left\{ k \sqrt{e_h} \mathcal{F}\{\delta^2 V_b\} + 2i \frac{\sqrt{e_h}}{k} \mathbf{k} \cdot \mathcal{F}\{\delta \nabla(\phi_b^{(2)} - \phi_b^{(1)})\} \right\}, \end{aligned} \quad (5.22)$$

where  $\phi_b^{(1)}$  and  $V^{(1)}$  are obtained from (5.18)–(5.19),  $V^{(2)}$  and  $\phi_b^{(2)}$  from (5.20)–(5.21) and  $e_h = \exp(-2kh)$ . The equations for  $V^{(1)}$ ,  $V^{(2)}$ ,  $V^{(3)}$  are valid on the exact position of the free surface. Similarly, the potential and normal velocity at the sea floor are evaluated on its exact position.

In Fructus and Grue<sup>45</sup> they studied the full expression for  $V$  and computed the difference in the resulting wave field using the full  $V$  and the approximation provided by  $V^{(3)}$ . For very strong tsunami waves propagating over long distance, they found (in that investigation) that the relative error in amplitude and phase at maximum was 0.0014 and  $0.07 \times 10^{-4}$ , respectively, and thus that  $V^{(3)}$  represents a most useful approximation for the practical evaluation of highly nonlinear and highly dispersive phenomena relating to tsunami waves. The formulation is valid up to the physical beach where numerical boundary conditions are applied.<sup>14</sup>

## 6. Short Wave Formation by Tsunami in Shallow Water

The natural disaster caused by the Indian Ocean tsunami on December 26, 2004 led to large number of recent publications on tectonics, earthquakes, tectonically generated water waves and wave run-up along the coast line.<sup>47–50</sup> We shall here not model the tsunami itself but rather simulate the motion that was observed when the long tsunami ran into the Strait of Malacca, generating undular bores in the shallow sea. We use equations (2.6) and (5.22) to model the nonlinear-dispersive process taking place during the formation of the short waves. The input wave to the simulation starting at the entrance of the Strait corresponds to a model simulation of the Indian Ocean tsunami.

The computations presented here represent a short summary of a fuller investigation where fully nonlinear-dispersive computations and a variant of the KdV equation were compared.<sup>51</sup> We perform a modeling along a 2D section that is midway between the Sumatra Island and Malaysian Peninsula. The depth profile of the sea ranges from 160 m at the starting

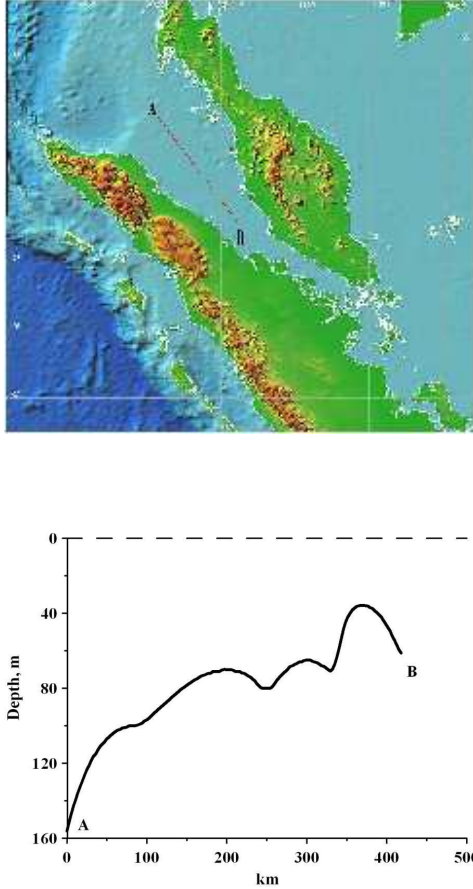


Fig. 14. Upper: computational section A–B in the Strait of Malacca. Lower: depth profile along section.

position and reduces to 80 m after 200 km, and to 37 m after 375 km (figure 14). The input wave has an initial depression period of about 1500 s, a maximal depression of  $-2.4$  m and a subsequent elevation of 2.8 m, see figure 16a. The numerical tank is 1430 km long. Two resolutions of 20 m and 40 m were used, meaning up to  $1.4 \cdot 10^5$  nodes, since there are always a minimum of two nodes in the lateral direction. An estimated wavelength of the train of short waves is about 400 m (see below) giving (about) 20 nodes per wavelength with the fine resolution and 10 with coarse, both producing same result.

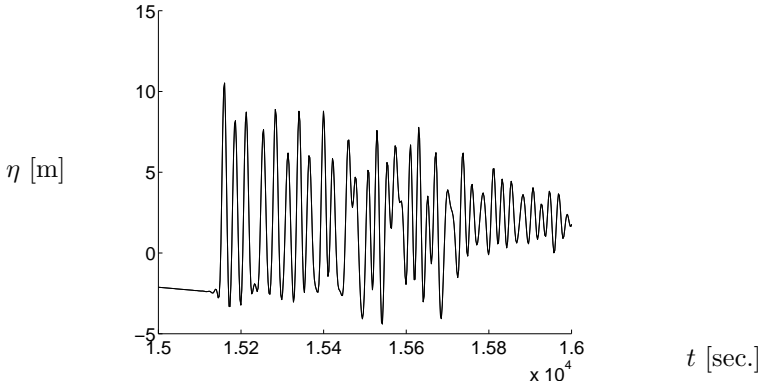


Fig. 15. Elevation vs. time at position 375 km from entrance of the Strait. Local water depth 37 m.

The back face of the leading depression wave undergoes a significant steepening during the propagation in the shallow strait, where the value of the vertical velocity has a local maximum of 0.008 m/s at the entrance, and reaches a local maximum of 0.4 m/s at the position at 250 km. A train of short waves then develops in the subsequent motion (figure 16c). The crest to crest period is in the beginning about half a minute, corresponding to peak frequency of  $\omega_p = 10^{-0.631} \text{ s}^{-1}$  in figure 16b, at 250 km.

The energy supply to the short waves comes from the steep back of the long, leading depression wave. In the beginning, the group of short waves has very small amplitude and behaves like a linear dispersive wave train. This fact is illustrated by plotting  $\partial\eta/\partial t$  as function of time (figure 16d). A close examination of the train of short waves supports that the local wave length during the generation phase is governed by the linear dispersion relation  $\omega^2 = gk \tanh kh$ ,  $h$  local depth. While the front of the train of short waves moves with the shallow water speed,  $\sqrt{gh}$ , the tail moves with the slower group velocity  $\partial\omega/\partial k$ . The train extends behind the steep front since  $\sqrt{gh} > \partial\omega/\partial k$ .

At the third bottom peak at 375 km and depth of 37 m, nondimensional wavenumber increases to  $kh \simeq 0.6$  ( $2\pi/k \simeq 400$  m) and wave height to depth ratio to 0.41, and the motion falls outside the range of validity of weakly nonlinear-dispersive theory. The train of short waves continues to grow in length and strength until the local wave height is about twice that of the incoming wave. The wave train develops into a sequence of solitary waves that propagate along the leading depression wave (figure 15). The

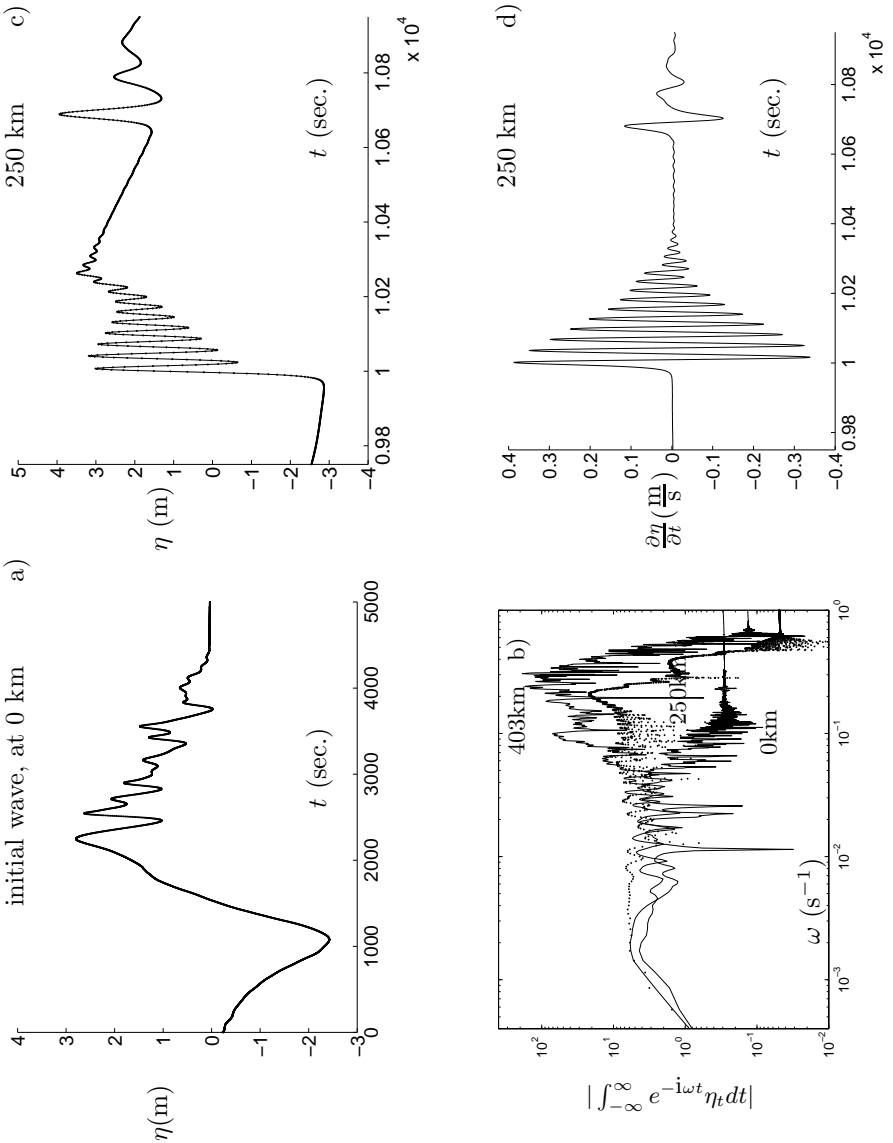


Fig. 16. a) Time history of surface elevation at the entrance of the Strait. b) Up-shift of energy by fully nonlinear-dispersive computations:  $|\int_{-\infty}^{\infty} e^{-i\omega t} \eta_t dt|$  vs.  $\omega$ . for 0 km (initial), 250 km, 403 km. c) Time history of  $\eta$  at 250 km and d) of  $\partial\eta/\partial t$  at 250 km.

transfer of energy from long to short modes shows a peak frequency at the position at 403 km of  $\omega_p = 10^{-0.514} \text{ s}^{-1}$ , corresponding to a wave period of 20.5 s (figure 16b). The motion due to an input wave of half amplitude exhibits a similar energy transfer taking place at the third bottom ridge. Finally, simulations using the fully nonlinear-dispersive formulation and a KdV model both support the formation of solitons in the shallow Strait of Malacca due to a disaster wave such as the Indian Ocean tsunami, but show that KdV is inferior in representing the short waves.<sup>51</sup>

## 7. Concluding Remarks

We have presented the mathematical description and numerical implementation of a fully nonlinear and dispersive model in three-dimensions. The essential parts of the method include a trimmed time-integration procedure of the free surface variables, the elevation,  $\eta$ , and wave potential at the free surface,  $\tilde{\phi}$ , where the quantities are evaluated in spectral space. In this integration, the linear contribution is obtained analytically, corresponding to one long time-step using the initial condition as input. The genuinely nonlinear motion is stepped forward in time using a RK-54 method with auto-adaptive time-step selection. Moreover, an anti-aliasing strategy has been implemented for multiplications up to cubic nonlinearities, where the spectra of the variables are doubled and energy at the highest half of the wavenumber nodes padded to zero.

The other important part is the analytical inversion of the Laplace equation expressing the normal velocity at the free surface in terms of  $\eta$  and  $\tilde{\phi}$ . This defines an analytical iteration method to obtain the fully nonlinear solution, with rapid convergence. The numerical counterpart of the method provides a highly efficient computational strategy where the dominant part of the evaluations are performed using FFT. A remaining part of the Laplace equation solver is obtained by highly nonlinear and local integrals where the integrands decay rapidly and are evaluated by ordinary integration over squares in the horizontal plane, with sides one characteristic wavelength. The method has been fully numerically implemented, convergence properties documented,<sup>13</sup> with wave generation and absorption procedures embedded.<sup>14</sup> Numerical integration of the evolution of long wave fields over long time using the two-dimensional counterpart of the method<sup>16</sup> showed excellent comparison with the high-order spectral method by West et al.,<sup>8</sup> but that the formulation by Dommermuth and Yue<sup>9</sup> was inaccurate at large times of the simulation, due to poor representation of the

vertical velocity at the free surface. The present method, particularly the pure FFT-part, is faster than other related methods.

Various wave phenomenas are computed, like formation of three-dimensional surface wave patterns, very large wave events caused by linear and nonlinear focusing, and short wave formation due to a long tsunami propagating into shallow water. The computations are illustrated in this chapter. We point to particularly three highlights. Firstly, a main objective with the present computations of three-dimensional patterns was to model the relatively obscure  $L_1$ -pattern – the oscillating horse shoes – observed by Collard and Caulliez<sup>27</sup> in a wave tank, which, until recently, was not given a theoretical explanation.<sup>28,30</sup> A reason why they observed the pattern was, first, that they suppressed the class I instability – the sideband instability – by putting in the wave tank a thin sheet of plastic-film on the water surface, and, secondly, the  $L_1$ -pattern was triggered because of parametric resonance taking place in the lateral motion in the wave tank, determining the value of the lateral wavenumber,  $qk_0$ . This  $L_1$ -pattern should be observed in coastal waters where the modulational instability becomes relatively weaker. For steep waves in deep water the strength of class II instability alone is sufficient to trigger breaking of the wave. In water of moderate depth, with  $kh = 1$ , class II instability dominates class I instability when  $(ak)_0 > 0.1$ , exhibits recurrence for  $0.1 < (ak)_0 < 0.13$ , and class II breaking for  $(ak)_0 > 0.13$ .

A second main result is the recomputation and experimental investigation of extremely large wave events corresponding to the largest waves that are documented at sea, namely the Camille and Draupner waves. Both are characterized by a maximal elevation above mean sea level,  $\eta_m$ , times an estimated local wavenumber of the event,  $k$ , with product  $k\eta_m = 0.49$ , for the waves in the field, where the procedure of how to obtain the local wavenumber is detailed in the text prior to equation (4.1). Recomputations of the high waves compare favorably with available sets of laboratory measurements using Laser Doppler Anemometry and Particle Image Velocimetry. Based on the simulations presented here one may conclude that the local properties of waves such as the large Camille and Draupner waves share a common kinematics and is obtained by simulation and experiment. Moreover, the results indicate that both the Camille and Draupner waves eventually developed into breaking at a later stage losing a substantial fraction of momentum and energy. (Waves with  $k\eta_m < 0.39$  and  $u/c < 0.45$  are recurrent and do not break.)

The third important point relates to the extension of the mathematical model and numerical implementation taking into account the effect of a general variable bottom in space and time. This expresses the free surface normal velocity and bottom potential in an FFT fashion of the involved variables. The formulation has an unexplored potential for further use in computation, application and interpretation.

The method requires  $\mathcal{O}(N \log N)$  operations per time-step,  $N$  the number of computational nodes. Computations so far are carried out on lap-tops using a typical resolution of 32 nodes per characteristic wavelength in both directions, which means  $10^3$  nodes per wavelength squared. In the largest computation of formation of extreme events, using the full method, a wave tank of 32 by 4 wavelengths was used, corresponding to a total number of nodes of  $N = 1.3 \cdot 10^5$ . In the computations of the short wave formation due to the tsunamis, the number of nodes was  $N = 1.4 \cdot 10^5$  in the finest computation, which involved only the rapid FFT-part of the formulation, since in this application the remaining integrals are vanishingly small. In the tsunami-wave application the number of nodes per wavelength was (about) 20 with the fine resolution and 10 with coarse. The wave propagation period was  $2 \cdot 10^4$  seconds corresponding to slightly less than 6 hours.

The code is implemented with version FFTW2.5 of the Fourier transform and with parallel architecture that awaits to be tested. An upgrade of the program using FFTW3 will divide the applied number of nodes by a factor of two. We believe that an upgrade of the code for runs on clusters represents a next step. From the application side the code should be used as support for interpretation of field data computing wave fields over areas, at least, 100 by 100 typical wavelengths, or more desirably, 1000 by 1000 wavelengths. The former means a number of  $N = 10^7$  nodes while the latter means  $10^9$  nodes, and is a factor  $10^2 - 10^4$  higher than in the computations pursued so far. This should be feasible, given available computer resources.

## Acknowledgements

We acknowledge the collaboration with Drs. Didier Clamond and Atle Jensen. The text was written when J.G. was on sabbatical leave at Scripps Institution of Oceanography in La Jolla, San Diego, USA. He expresses his gratitude to Professor W. Kendall Melville and his group for making the visit possible and most beneficial. Development of the method was funded by the Research Council of Norway through: NFR 146526/420 *General analysis of Realistic Ocean Waves (GROW)* 1998-2002,

NFR 121078/420 *Modelling of currents and waves for sea structures 2002-6*, and BeMatA-program *Computational methods for stratified flows involving internal waves*.

## References

1. Benjamin, T. B. and Feir, J. E. (1967). The disintegration of wave trains on deep water. *J. Fluid Mech.*, **27**, pp. 417–430.
2. Zakharov, V. E. (1968). Stability of periodic wave of finite amplitude on the surface of a deep fluid. *J. Appl. Mech. Phys., Engl. Transl*, **2**, p. 190.
3. Yuen, H. C. and Lake, B. M. (1982). Nonlinear dynamics of deep-water gravity waves. *Adv. Appl. Mech.*, **22**, pp. 67–229.
4. Tayfun, M. (1980). Narrow-band nonlinear sea waves. *J. Geophys. Res.*, **85**, C3, pp. 1548–1552.
5. Onorato, M., Osborne, A. R. and Serio, M. (2002). Extreme wave events in directional, random oceanic sea states. *Phys. Fluids*, **14**, pp. L25–L28.
6. Dysthe, K. B., Trulsen, K., Krogstad, H. E. and Socquet-Juglard, H. (2003). Evolution of a narrow-band spectrum of random surface gravity waves. *J. Fluid Mech.*, **478**, pp. 1–10.
7. Socquet-Juglard, H., Dysthe, K. B., Trulsen, K., Krogstad, H. E. and Liu, J. (2005). Distribution of surface gravity waves during spectral changes. *J. Fluid Mech.*, **542**, pp. 195–216.
8. West, B. J., Brueckner, K. A., Janda, R. S., Milder, D. M. and Milton, R. L. (1987). A new numerical method for surface hydrodynamics. *J. Geophys. Res.* **92**, 11, pp. 11803–11824.
9. Dommermuth, D. G. and Yue, D. K. P. (1987). A high-order spectral method for the study of nonlinear gravity waves. *J. Fluid Mech.*, **184**, pp. 267–288.
10. Craig, W. and Sulem, C. (1993). Numerical simulation of gravity waves. *J. Comp. Phys.* **108**, pp. 73–83.
11. Clamond, D. and Grue, J. (2001). A fast method for fully nonlinear water-wave computations. *J. Fluid Mech.*, **447**, pp. 337–355.
12. Grue, J. (2002). On four highly nonlinear phenomena in wave theory and marine hydrodynamics. *Appl. Ocean Res.*, **24**, pp. 261–274.
13. Fructus, D., Clamond, D., Grue, J. and Kristiansen, Ø. (2005). An efficient model for three-dimensional surface wave simulations. Part I. Free space problems. *J. Comp. Phys.* **205**, pp. 665–685.
14. Clamond, D., Fructus, D., Grue, J. and Kristiansen, Ø. (2005). An efficient model for three-dimensional surface wave simulations. Part II: Generation and absorption. *J. Comp. Phys.*, **205**, pp. 686–705.
15. Clamond, D., Fructus, D. and Grue, J. (2007). A note on time integrators in water-wave simulations. *J. Eng. Math.*, **58**, pp. 149–156. Special issue in honor of Prof. J. N. Newman.
16. Clamond, D., Francius, M., Grue, J. and Kharif, Ch. (2006). Long time interaction of envelope solitons and freak wave formations. *Eur. J. Mech. B/Fluids*, **25**, pp. 536–553.

17. Grue, J. and Trulsen, K. (eds.) (2006). Waves in Geophysical Fluids; Tsunamis, Rogue Waves, Internal Waves and Internal Tides. CISM lectures, Vol. 489, Springer 332 pp.
18. Lighthill, M. J. (1965). Contributions to the theory of waves in nonlinear dispersive systems. *J. Fluid Mech.*, **183**, pp. 451-465.
19. Su, M. Y. (1982). Three-dimensional deep water waves. Part 1. Experimental measurements of skew and symmetric wave patterns. *J. Fluid Mech.*, **124**, pp. 73-108.
20. McLean, J. W., Ma, Y. C., Martin, D. U., Saffman, P. G. and Yuen, H. C. (1981). Three dimensional instability of finite amplitude water waves. *Phys. Rev. Letters*, **46**, pp. 817-820.
21. McLean, J. W. (1982). Instabilities of finite-amplitude water waves. *J. Fluid Mech.*, **114**, pp. 315-330.
22. Longuet-Higgins, M. S. (1978). The instabilities of gravity waves of finite amplitude in deep water. II. Subharmonics. *Proc. R. Soc. Lond. A*, **360**, pp. 489-505.
23. Kharif, C. and Ramamonjariisoa, A. (1988). Deep-water gravity waves instabilities at large steepness. *Phys. Fluids*, **31**, pp. 1286-1288.
24. Kharif, C. and Ramamonjariisoa, A. (1990). On the stability of gravity waves on deep water. *J. Fluid Mech.*, **218**, pp. 163-170.
25. Melville, W. K. (1982). The instability and breaking of deep-water waves. *J. Fluid Mech.*, **115**, pp. 165-185.
26. Kusuba, T. and Mitsuyasu, M. (1986). Nonlinear instability and evolution of steep water waves under wind action. *Rep. Res. Inst. Appl. Mech. Kyushu Univ.* **33**, (101), pp. 33-64.
27. Collard, F. and Caulliez, G., 1999. Oscillating crescent-shaped water wave patterns. *Phys. Fluids, Letters*, **11**, pp. 3195-3197.
28. Fructus, D., Kharif, Ch., Francius, M., Kristiansen, Ø, Clamond, D. and Grue, J. (2005). Dynamics of crescent water wave patterns. *J. Fluid Mech.*, **537**, pp. 155-186.
29. Xue, M., Xü, H., Liu Y. M. and Yue, D. K. P. (2001). Computations of fully nonlinear three-dimensional wave-wave and wave-body interactions. Part 1. Dynamics of steep three-dimensional waves. *J. Fluid Mech.*, **438**, pp. 11-39.
30. Fuhrman, D. R., Madsen P. A. and Bingham H. B. (2004). A numerical study of crescent waves. *J. Fluid Mech.*, **513**, pp. 309-342.
31. Fenton, J. D. (1988). The numerical solution of steady water wave problems. *Computers Geosci.* **14**, pp. 357-368.
32. Skandrani, C. (1996). Contribution à l'étude de la dynamique non linéaire de champs de vagues tridimensionnels en profondeur infinie. PhD thesis, Univ. de la Méditerranée.
33. Su, M. Y. and Green, A. W. (1984). Coupled two- and three-dimensional instabilities of surface gravity waves. *Phys. Fluids*, **27**, pp. 2595-2597.
34. M. Francius and C. Kharif (2006). Three-dimensional instabilities of periodic gravity waves in shallow water. *J. Fluid Mech.*, **561**, pp. 417-437.
35. Kristiansen, Ø., Fructus, D., Clamond, D. and Grue, J. (2005). Simulations of crescent water wave patterns on finite depth. *Phys. Fluids.*, **17**, 064101-1-15.

36. Clamond, D. and Grue, J. (2002). Interaction between envelope solitons as a model for freak wave formations. Part I: Long time interaction. *C. R. Mecanique*, **330**, pp. 575–580.
37. Ochi, M. K. (1998). Ocean waves - the stochastic approach. Camb. Univ. Press. 320 pp.
38. Trulsen, K. (1999). *Trans. ASME*, **121**, pp. 126-130.
39. Kharif, C. and Pelinovsky, E. (2003). Physical mechanisms of the rogue wave phenomenon. *Eur. J. Mech. B/Fluids*, **22**, pp. 603-634.
40. Grue, J., Clamond, D., Huseby, M. and Jensen, A. (2003). Kinematics of extreme waves in deep water. *Appl. Ocean Res.*, **25**, pp. 355-366.
41. Grue, J. and Jensen, A. (2006). Experimental velocities and accelerations in very steep wave events in deep water. *Eur. J. Mech. B/Fluids*, **25**, pp. 554-564.
42. Dold, J. W. & Peregrine, D. H., 1986. Water-wave modulation. *Proc. 20th Int. Conf. on Coastal Engineering*, American Society of Civil Engineers, Taipei, 10-14 Nov. 1986, 163–175.
43. Banner, M. L. and Tian, X. (1998). On the determination of the onset of breaking for modulating surface water waves. *J. Fluid Mech.*, **367**, pp. 107-137.
44. Baldock, T. E., Swan, C. and Taylor, P. H. (1996). A laboratory study of nonlinear surface waves on water. *Phil. Trans. R. Soc. A*, Vol. 354, *Phil. Trans. R. Soc. A*, **354**, pp. 649-676.
45. Fructus, D. and Grue, J. (2007). An explicit method for the nonlinear interaction between water waves and variable and moving bottom topography. *J. Comp. Phys.*, **222**, pp. 720-739.
46. Hammack, J. (1973). A note on tsunamis: their generation and propagation in an ocean of uniform depth. *J. Fluid Mech.*, **60**, pp. 769–700.
47. Liu, P. L.-F. (2005). Tsunami simulations and numerical models. *The Bridge (National Academy of Sciences, USA)*, **35**, (2), pp. 14-20.
48. Dalrymple, R. A., Grilli, S. T. and Kirby, J. T. (2006). Tsunamis and challenges for accurate modeling. *Oceanography I*, **19**, (1), pp. 142-151.
49. Glimsdal, S., Pedersen, G. K., Atakan, K., Harbitz, C. B., Langtangen, H. P. and Løvholt, F. (2006). Propagation of the Dec. 26, 2004, Indian Ocean Tsunami: Effects of Dispersion and Source Characteristics. *Int. J. Fluid Mech. Res.* **33**, (1), pp. 15-43.
50. Pelinovsky, E. N. (2006). Hydrodynamics of tsunami waves. In: *Waves in geophysical fluids. Tsunamis, rogue waves, internal waves and internal tides*, J. Grue and K. Trulsen (Eds.), CISM courses and lecture series No. 489, Springer, 2006, pp. 1-48.
51. Grue, J., Pelinovsky, E. N., Fructus, D., Talipova, T. and Kharif, Ch. (2008). Formation of undular bores and solitary waves in the Strait of Malacca caused by the Dec. 26, 2004, Indian Ocean tsunami. *J. Geophys. Res.* (in press).